ATLAS CONF Note

ATLAS-CONF-2018-012

20th May 2018

Correlated long-range mixed-harmonic fluctuations in pp, p+Pb and low-multiplicity Pb+Pb collisions with the ATLAS detector

The ATLAS Collaboration

Correlations of two flow harmonics v_n and v_m via three- and four-particle cumulants are measured in 13 TeV pp, 5.02 TeV p+Pb, and 2.76 TeV peripheral Pb+Pb collisions with the ATLAS detector at the LHC. The goal is to understand the multi-particle nature of the long-range collective phenomenon in these collision systems. The large non-flow background from dijet production present in the standard cumulant method is suppressed using a method of subevent cumulants involving two, three and four pseudorapidity-separated subevents. The results show an anti-correlation between v_2 and v_3 and a positive correlation between v_2 and v_4 for all collision systems and over the full multiplicity range. However, the magnitudes of the correlations are found to depend strongly on the event multiplicity, the choice of the transverse momentum range and the collision systems. The relative correlation strength, obtained by normalization of the cumulants with the $\langle v_n^2 \rangle$ from a two-particle correlation analysis, is similar in the three collision systems and depends weakly on the event multiplicity and transverse momentum. The new results based on the subevent methods provide strong evidence for a similar long-range multi-particle collectivity in pp, p+Pb and peripheral Pb+Pb collisions.

ATLAS-CONF-2018-012
21 May 2018

1 Introduction

One of the goals in the studies of azimuthal correlations in high-energy nuclear collisions at the Relativistic Heavy Ion Collider (RHIC) and the Large Hadron Collider (LHC) is to understand the multi-parton dynamics of QCD in the strongly coupled non-perturbative regime [1]. Measurements of azimuthal correlations in small collision systems, such as pp, p+A or d+A collisions, have revealed the ridge phenomenon [2–6]: enhanced production of particle pairs at small azimuthal angle separation, $\Delta\phi$, extended over a wide range of pseudorapidity separation, $\Delta\eta$. The azimuthal structure has been related to harmonic modulation of particle densities, characterized by a Fourier expansion, $\mathrm{d}N/\mathrm{d}\phi \propto 1 + 2\sum_{n=1}^{\infty} v_n \cos n(\phi - \Phi_n)$, where v_n and Φ_n represent the magnitude and the event-plane angle of the n^{th}-order flow harmonic. The v_n are known to depend on the collision system, but have weak dependence on collision energies [6, 7]. The ridge reflects multi-parton dynamics early in the collision and has generated significant interest in the high-energy physics community. A key question is the timescale for the emergence of the long-range multi-particle collectivity, for instance, whether it reflects initial momentum correlation from gluon saturation effects [8], or a final-state hydrodynamic response to the initial transverse collision geometry [9].

Further insight about the ridge phenomenon is obtained via a multi-particle correlation technique, known as cumulants, involving three or more particles [10–12]. The multi-particle cumulants probe the event-by-event fluctuation of a single flow harmonic v_n, as well as the correlated fluctuations between two flow harmonics, v_n and v_m. These event-by-event fluctuations are often represented by probability density distributions $p(v_n)$ and $p(v_n, v_m)$, respectively. For instance, the four-particle cumulants $c_n\{4\} = \left\langle v_n^4 \right\rangle - 2\left\langle v_n^2 \right\rangle^2$ constrain the width of $p(v_n)$ [10], while the four-particle symmetric cumulants $\mathrm{sc}_{n,m}\{4\} = \left\langle v_n^2 v_m^2 \right\rangle - \left\langle v_n^2 \right\rangle \left\langle v_m^2 \right\rangle$ quantify the lowest-order correlation between v_n and v_m [12]. The three-particle "asymmetric cumulants" such as $\mathrm{ac}_n\{3\} = \left\langle v_n^2 v_{2n} \cos 2n(\Phi_n - \Phi_{2n}) \right\rangle$ [5, 13] are sensitive to correlations involving both the flow magnitude v_n and flow phase Φ_n.

One of the challenges in the study of azimuthal correlations in small collision systems is how to distinguish the long-range ridge from sources of "non-flow" contribution involving only a few particles, such as resonance decays, jets, or dijets. For two-particle correlations, the non-flow contribution is commonly suppressed by requiring a large $\Delta\eta$ gap between the two particles in each pair and a peripheral subtraction procedure [3–5, 7, 14, 15]. For multi-particle cumulants, the non-flow contributions can be suppressed by requiring correlation between particles from different subevents separated in η, while preserving the genuine long-range multi-particle correlations associated with the ridge. Here each subevent is a collection of particles in a given η range. This so-called "subevent method" has been demonstrated to reliably measure $c_n\{4\}$ and $\mathrm{sc}_{n,m}\{4\}$ [13, 16]. In contrast, $c_n\{4\}$ and $\mathrm{sc}_{n,m}\{4\}$ based on the standard cumulant method are contaminated by non-flow correlations over the full multiplicity range in pp collisions and the low multiplicity region in p+A collisions [16]. In small collision systems, measurements have been performed for $c_n\{4\}$ with both the standard [15, 17] and subevent methods [18], and for $\mathrm{sc}_{n,m}\{4\}$ with the standard method [19]. The subevent method has not yet been used to measure $\mathrm{sc}_{n,m}\{4\}$, and no measurements of $\mathrm{ac}_n\{3\}$ have ever been attempted in small collision systems.

This paper presents measurements of $\mathrm{sc}_{2,3}\{4\}$, $\mathrm{sc}_{2,4}\{4\}$ and $\mathrm{ac}_2\{3\}$ in pp collisions at $\sqrt{s}$ = 13 TeV, p+Pb collisions at $\sqrt{s_{\mathrm{NN}}}$ = 5.02 TeV and low-multiplicity Pb+Pb collisions at $\sqrt{s_{\mathrm{NN}}}$ = 2.76 TeV. They are obtained using two-, three- and four-subevent cumulant methods and are compared to the standard cumulant method. The cumulants are normalized by the $\left\langle v_n^2 \right\rangle$ obtained from a two-particle correlation analysis [7] to quantify their relative correlation strength. The measurements suggest that the results obtained with standard method are strongly contaminated by correlations from non-flow sources. The

results obtained with the three-subevent method or the four-subevent method provide new evidence for long-range three- or four-particle azimuthal correlations.

The paper is organized as follows. Details of the ATLAS detector, the trigger system, datasets, as well as event and track selections are provided in Sections 2 to 4. Section 5 describes the standard and subevent cumulant methods used in this analysis. The correlation analysis and systematic uncertainties are described in Sections 6 and 7, respectively. The measured cumulants are presented in Section 8. A summary is given in Section 9.

2 Detector and trigger

The ATLAS detector [20] provides nearly full solid-angle coverage around the collision point with tracking detectors, calorimeters, and muon chambers, and is well suited for measurement of multi-particle correlations over a large pseudorapidity range[1]. The measurements were performed primarily using the inner detector (ID), minimum-bias trigger scintillators (MBTS) and the zero-degree calorimeters (ZDC). The ID detects charged particles within $|\eta| < 2.5$ using a combination of silicon pixel detector, a silicon microstrip detector (SCT), and a straw-tube transition radiation tracker, all immersed in a 2 T axial magnetic field [21]. An additional pixel layer, the "insertable B-layer" (IBL) [22] installed between Run 1 period (2010–2013) and Run 2 period (2015–2018), is available for the Run 2 datasets. The MBTS detects charged particles within $2.1 \lesssim |\eta| \lesssim 3.9$ using two hodoscopes of counters positioned at $z = \pm\ 3.6$ m. The ZDC, used only in p+Pb and Pb+Pb collisions, are positioned at ±140 m from the collision point, and detect neutral particles, primarily neutrons and photons, with $|\eta| > 8.3$.

The ATLAS trigger system [23,24] consists of a Level-1 (L1) trigger implemented using a combination of dedicated electronics and programmable logic, and a high-level trigger (HLT) implemented in processors. The HLT reconstructs charged-particle tracks using methods similar to those applied in the offline analysis. The HLT enables the high-multiplicity track triggers (HMT) to select events based on the number of tracks having $p_{\mathrm{T}} > 0.4$ GeV associated with the primary vertex. The different HMT triggers apply additional requirements on either the total transverse energy (E_{T}) in the calorimeters or on the number of hits in the MBTS by the L1 trigger, and on the number of reconstructed charged-particle tracks associated to the primary vertex by the HLT trigger, while the pp and p+Pb data were collected using combination of the minimum-bias and HMT triggers. The minimum-bias trigger required either a hit in at least one MBTS counter, or a hit in at least one MBTS counter on each side, or at least one reconstructed track at the HLT seeded by a random trigger at L1. More detailed information on the triggers and their performance used for the pp and p+Pb data can be found in Refs. [7,25] and Refs. [5,26], respectively.

3 Datasets and Monte Carlo simulations

This analysis is based on ATLAS datasets corresponding to integrated luminosities of 0.9 pb^{-1} of pp data recorded at $\sqrt{s}$ = 13 TeV, 28 nb^{-1} of p+Pb data recorded at $\sqrt{s_{\mathrm{NN}}}$ = 5.02 TeV, and 7 μb^{-1} of Pb+Pb

[1] ATLAS typically uses a right-handed coordinate system with its origin at the nominal interaction point (IP) in the center of the detector and the z-axis along the beam pipe. The x-axis points from the IP to the center of the LHC ring, and the y-axis points upward. Cylindrical coordinates (r, ϕ) are used in the transverse plane, ϕ being the azimuthal angle around the beam pipe. By default, the pseudorapidity is defined in terms of the polar angle θ as $\eta = -\ln\tan(\theta/2)$. However, for asymmetric p+Pb or Pb+p collisions, the $-z$ direction is always defined as the direction of the Pb beam.

data at $\sqrt{s_{\mathrm{NN}}}$ = 2.76 TeV. The 2.76 TeV Pb+Pb data were collected in 2010. The p+Pb data were mainly collected in 2013, but also include 0.3 nb^{-1} of data collected in 2016, which increase the number of events at moderate multiplicity (see Section 4). During both p+Pb runs, the LHC was configured to provide a 4 TeV proton beam and a 1.57 TeV per-nucleon Pb beam, which produced collisions at $\sqrt{s_{\mathrm{NN}}}$ = 5.02 TeV, with a rapidity shift of 0.465 of the nucleon–nucleon center-of-mass frame towards the proton beam direction relative to the ATLAS rest frame. The direction of the Pb beam is always defined to have negative pseudorapidity. The 13 TeV pp data were collected during several special low-pileup runs of the LHC in 2015 and 2016. A summary of the datasets used in this analysis is shown in Table 1.

Table 1: The list of datasets used in this analysis.

	Pb+Pb	p+Pb	pp
integrated luminosity (year)	7 μb^{-1} (2010)	28 nb^{-1} (2013)	0.07 pb^{-1} (2015)
		0.3 nb^{-1} (2016)	0.84 pb^{-1} (2016)

The track reconstruction efficiency was determined using simulated Monte Carlo (MC) event samples (Section 4). The pp events were simulated with the Pythia8 MC event generator [27] using the A2 tune parameters with MSTW2008LO parton distribution functions [28]. The HIJING event generator [29] was used to produce Pb+Pb and p+Pb collisions with the same energy and the same boost of the center-of-mass system as in the data. The detector response was simulated using Geant4 [30,31] with detector conditions matching those during the data-taking. The simulated events and data events are reconstructed with the same algorithms. The MC sample for Pb+Pb events in the multiplicity region of interest was very small, therefore the reconstruction efficiency for Pb+Pb was taken from the larger p+Pb sample reconstructed with the same track reconstruction algorithm. The p+Pb efficiency was found to be consistent with efficiency from the Pb+Pb MC simulation [17].

4 Event and track selection

The offline event selection for the pp and p+Pb data requires at least one reconstructed vertex with its longitudinal position satisfying $|z_{\mathrm{vtx}}| < 100$ mm relative to the nominal interaction point. The vertex is required to have at least two associated tracks with $p_{\mathrm{T}} > 0.4$ GeV. The mean number of collisions per bunch crossing, μ, was 0.002–0.8 for the 13 TeV pp data, 0.03 for the 2013 p+Pb data, 0.001–0.006 for the 2016 p+Pb data. In order to suppress additional interactions in the same bunch crossing (referred to as pileup) in pp collisions, events containing additional vertices with at least four associated tracks are rejected. In p+Pb collisions, events with more than one good vertex, defined as any vertex for which the scalar sum of the p_{T} of the associated tracks is greater than 5 GeV, are rejected. The remaining pileup events are further suppressed by using the signal in the ZDC on the direction of Pb beam. This signal is calibrated to the number of detected neutrons, N_n, by using the location of the peak corresponding to a single neutron. The distribution of N_n in events with pileup is broader than that for the events without pileup. Hence a simple requirement on the ZDC signal distribution is used to further suppress events with pileup, while retaining more than 98% of events without pileup. The impact of residual pileup, at the level of $\lesssim 10^{-3}$, is studied by comparing the results obtained from data with different μ values.

The offline event selection for the Pb+Pb data requires $|z_{\mathrm{vtx}}| < 100$ mm. The selection also requires a time difference $|\Delta t| < 3$ ns between signals in the MBTS trigger counters on either side of the interaction point to suppress non-collision backgrounds. A coincidence between the ZDC signals at forward and backward

pseudorapidity is required to reject a variety of background processes, while maintaining high efficiency for inelastic processes. The fraction of events with more than one interaction after these selection criteria is less than 10^{-4}.

Charged-particle tracks and collision vertices are reconstructed using algorithms optimized for improved performance for LHC Run 2. In order to compare directly with the pp and p+Pb systems using event selections based on the multiplicity of the collisions, a subset of data from low-multiplicity Pb+Pb collisions, collected during the 2010 LHC heavy-ion run with a minimum-bias trigger, was analyzed using the same track reconstruction algorithm as that used for p+Pb collisions. For the Pb+Pb and 2013 p+Pb analyses, tracks are required to have a p_{T}-dependent minimum number of hits in the SCT. The transverse (d_0) and longitudinal ($z_0 \sin\theta$) impact parameters of the track relative to the vertex are required to be less than 1.5 mm. Additional requirements $|d_0|/\sigma_{d_0} < 3$ and $|z_0 \sin\theta|/\sigma_{z_0} < 3$ are imposed, where σ_{d_0} and σ_{z_0} are the uncertainties on the transverse and longitudinal impact parameter values, respectively. A more detailed description of the track selection for the 2010 Pb+Pb data and 2013 p+Pb data can be found in Refs. [5, 17].

For all the data taken since the start of Run 2, the track selection criteria make use of the IBL, as described in Refs. [14, 25]. Furthermore, the requirements of $|d_0^{\mathrm{BL}}| < 1.5$ mm and $|z_0 \sin\theta| < 1.5$ mm are applied, where d_0^{BL} is the transverse impact parameter of the track relative to the beam line (BL).

The cumulants are calculated using tracks passing the above selection requirements, and having $|\eta| < 2.5$ and $0.3 < p_{\mathrm{T}} < 3$ GeV or $0.5 < p_{\mathrm{T}} < 5$ GeV. These two p_{T} ranges are chosen because they were often used in the previous ridge measurements at the LHC [6, 7, 14, 15, 17]. However, to count the number of reconstructed charged particles for event-class definition (denoted by $N_{\mathrm{ch}}^{\mathrm{rec}}$), tracks with $p_{\mathrm{T}} > 0.4$ GeV and $|\eta| < 2.5$ are used for compatibility with the requirements in the HLT selections described above. Due to different trigger requirements, most of the p+Pb events with $N_{\mathrm{ch}}^{\mathrm{rec}} > 150$ are provided by the 2013 dataset, while the 2016 dataset provides most of the events at lower $N_{\mathrm{ch}}^{\mathrm{rec}}$.

The efficiency of the combined track reconstruction and selection requirements in data is estimated using MC samples reconstructed with the same tracking algorithms and track selection requirements. Efficiencies, $\epsilon(\eta, p_{\mathrm{T}})$, are evaluated as a function of track η, p_{T} and the number of reconstructed charged-particle tracks, but averaged over the full range in azimuth. The efficiencies are similar for events with the same multiplicity. For all collision systems, the efficiency increases by about 4% as track p_{T} increases from 0.3 GeV to 0.6 GeV. Above 0.6 GeV, the efficiency is independent of p_{T} and reaches 86% (72%) for Run 1 pp and p+Pb, and 83% (70%) for Pb+Pb and Run 2 p+Pb collisions, at $\eta \approx 0$ ($|\eta| > 2$). The efficiency is independent of the event multiplicity for $N_{\mathrm{ch}}^{\mathrm{rec}} > 40$. For lower-multiplicity events the efficiency is smaller by up to 3% due to broader d_0 and $z_0 \sin\theta$ distributions [17].

The fraction of falsely reconstructed charged-particle tracks is also estimated and found to be negligibly small in all datasets. This fraction decreases with increasing track p_{T}, and even at the lowest transverse momenta of 0.2 GeV it is below 1% of the total number of tracks. Therefore, there is no correction for the presence of such tracks in the analysis.

In the simulated events, the reconstruction efficiency reduces the measured charged-particle multiplicity relative to the generated multiplicity for primary charged particles. The multiplicity correction factor b is used to correct $N_{\mathrm{ch}}^{\mathrm{rec}}$ to obtain the efficiency-corrected average number of charged particles per event, $\langle N_{\mathrm{ch}} \rangle = b \left\langle N_{\mathrm{ch}}^{\mathrm{rec}} \right\rangle$. The value of the correction factor is obtained from the MC samples described above, and is found to be independent of $N_{\mathrm{ch}}^{\mathrm{rec}}$ in the range used in this analysis, $N_{\mathrm{ch}}^{\mathrm{rec}} < 400$. Its value and the associated uncertainties are $b = 1.29 \pm 0.05$ for the Pb+Pb and 2013 p+Pb collisions and $b = 1.18 \pm 0.05$

for Run 2 p+Pb and pp collisions [32]. Both $\mathrm{sc}_{n,m}\{4\}$ and $\mathrm{ac}_2\{3\}$ are then studied as a function of $\langle N_{\mathrm{ch}}\rangle$.

5 Cumulant method

The multi-particle cumulant method [10] has the advantage of directly reducing non-flow correlations from jets and dijets. The mathematical framework for the standard cumulant is based on the Q-cumulants discussed in Refs. [11, 12, 33]. It has been recently extended to the case of subevent cumulants in Refs. [13, 16]. These methods are briefly summarized below.

5.1 Cumulants in the standard method

The standard cumulant method calculates k-particle azimuthal correlations, $\langle\{k\}\rangle$, in one event using a complex number notation [11, 12]:

$$\langle\{2\}_n\rangle = \left\langle e^{in(\phi_1-\phi_2)}\right\rangle \,,\; \langle\{3\}_n\rangle = \left\langle e^{i(n\phi_1+n\phi_2-2n\phi_3)}\right\rangle \,,\; \langle\{4\}_{n,m}\rangle = \left\langle e^{in(\phi_1-\phi_2)+im(\phi_3-\phi_4)}\right\rangle \,, \tag{1}$$

where "$\langle\rangle$" denotes a single-event average over all pairs, triplets or quadruplets, respectively. The averages from Eq. (1) can be expressed in terms of per-particle normalized flow vectors $\boldsymbol{q}_{n;l}$ with $l = 1, 2\ldots$ in each event [11]:

$$\boldsymbol{q}_{n;l} \equiv \sum_j w_j^l e^{in\phi_j} \Big/ \sum_j w_j^l \,, \tag{2}$$

where the sum runs over all tracks in the event and w_j is a weight assigned to the j^{th} track. This weight is constructed to correct for both detector non-uniformity and tracking inefficiency as explained in Section 6.

The multi-particle symmetric and asymmetric cumulants are obtained from $\langle\{k\}\rangle$ as:

$$\mathrm{ac}_n\{3\} = \langle\langle\{3\}_n\rangle\rangle \,,\; \mathrm{sc}_{n,m}\{4\} = \langle\langle\{4\}_{n,m}\rangle\rangle - \langle\langle\{2\}_n\rangle\rangle\langle\langle\{2\}_m\rangle\rangle \,, \tag{3}$$

where "$\langle\langle\rangle\rangle$" represents a weighted average of $\langle\{k\}\rangle$ over an event ensemble with similar $N_{\mathrm{ch}}^{\mathrm{rec}}$. One averages first over all distinct pairs, triplets or quadruplets in one event to obtain $\langle\{2\}_n\rangle$, $\langle\{2\}_m\rangle$, $\langle\{3\}_n\rangle$ and $\langle\{4\}_{n,m}\rangle$. Then they are averaged over an event ensemble with similar $N_{\mathrm{ch}}^{\mathrm{rec}}$ to obtain $\mathrm{sc}_{n,m}\{4\}$ and $\mathrm{ac}_n\{3\}$. In the absence of non-flow correlations, $\mathrm{sc}_{n,m}\{4\}$ and $\mathrm{ac}_n\{3\}$ measure the correlation between v_n and v_m or between v_n and v_{2n}:

$$\mathrm{ac}_n\{3\} = \left\langle v_n^2 v_{2n}\cos 2n(\Phi_n - \Phi_{2n})\right\rangle \,,\; \mathrm{sc}_{n,m}\{4\} = \left\langle v_n^2 v_m^2\right\rangle - \left\langle v_n^2\right\rangle\left\langle v_m^2\right\rangle \,. \tag{4}$$

This analysis measures three types of cumulants defined in Eq. (3): $\mathrm{sc}_{2,3}\{4\}$, $\mathrm{sc}_{2,4}\{4\}$ and $\mathrm{ac}_2\{3\}$.

5.2 Cumulants in the subevent method

In the "standard" cumulant method described above, all k-particle multiplets involved in $\langle\{k\}_n\rangle$ and $\langle\{k\}_{n,m}\rangle$ are selected using tracks in the entire ID acceptance of $|\eta| < \eta_{\max} = 2.5$. To further suppress the non-flow correlations that typically involve a few particles within a localized region in η, the tracks are divided into several subevents, each covering a unique η interval. The multi-particle correlations are then constructed by only correlating tracks between different subevents.

In the two-subevent cumulant method, the tracks are divided into two subevents, labelled by a and b, according to $-\eta_{\max} < \eta_a < 0$ and $0 \le \eta_b < \eta_{\max}$. The per-event k-particle azimuthal correlations are evaluated as:

$$\langle\{2\}_n\rangle_{a|b} = \left\langle e^{in(\phi_1^a - \phi_2^b)} \right\rangle, \langle\{3\}_n\rangle_{2a|b} = \left\langle e^{i(n\phi_1^a + n\phi_2^a - 2n\phi_3^b)} \right\rangle, \langle\{4\}_{n,m}\rangle_{2a|2b} = \left\langle e^{in(\phi_1^a - \phi_2^b) + im(\phi_3^a - \phi_4^b)} \right\rangle, \tag{5}$$

where the superscript or subscript a (b) indicates tracks chosen from the subevent a (b). Here the three- and four-particle cumulants are defined as:

$$\mathrm{ac}_n^{2a|b}\{3\} = \langle\langle\{3\}_n\rangle\rangle_{2a|b} \ , \ \mathrm{sc}_{n,m}^{2a|2b}\{4\} = \langle\langle\{4\}_{n,m}\rangle\rangle_{2a|2b} - \langle\langle\{2\}_n\rangle\rangle_{a|b} \langle\langle\{2\}_m\rangle\rangle_{a|b} \ . \tag{6}$$

The two-subevent method suppresses correlations within a single jet (intra-jet correlations), since particles from one jet usually fall in one subevent.

In the three-subevent cumulant method, tracks in each event are divided into three subevents a, b and c each covering one third of the η range, for example $-\eta_{\max} < \eta_a < -\eta_{\max}/3$, $|\eta_b| \le \eta_{\max}/3$ and $\eta_{\max}/3 < \eta_c < \eta_{\max}$. The multi-particle azimuthal correlations and cumulants are then evaluated as:

$$\langle\{3\}_n\rangle_{a,b|c} = \left\langle e^{i(n\phi_1^a + n\phi_2^b - 2n\phi_3^c)} \right\rangle \ , \ \langle\{4\}_{n,m}\rangle_{a,b|2c} = \left\langle e^{in(\phi_1^a - \phi_2^c) + im(\phi_3^b - \phi_4^c)} \right\rangle \ , \tag{7}$$

and

$$\mathrm{ac}_n^{a,b|c}\{3\} = \langle\langle\{3\}_n\rangle\rangle_{a,b|c} \ , \ \mathrm{sc}_{n,m}^{a,b|2c}\{4\} = \langle\langle\{4\}_{n,m}\rangle\rangle_{a,b|2c} - \langle\langle\{2\}_n\rangle\rangle_{a|c} \langle\langle\{2\}_m\rangle\rangle_{b|c} \ . \tag{8}$$

Since a dijet event usually produces particles in at most two subevents, the three-subevent method efficiently suppresses the non-flow contribution from inter-jet correlations associated with dijets. To maximize the statistical precision, the η range for subevent a is swapped with that for subevent b or c, and the results are averaged to obtain the final values.

The four-subevent cumulant method is only relevant for the symmetric cumulants $\mathrm{sc}_{n,m}\{4\}$. Tracks in each event are divided into four subevents a, b, c, and d, each covering one quarter of the η range: $-\eta_{\max} < \eta_a < -\eta_{\max}/2$, $-\eta_{\max}/2 \le \eta_a < 0$, $0 \le \eta_a < \eta_{\max}/2$, and $\eta_{\max}/2 \le \eta_d < \eta_{\max}$. The multi-particle azimuthal correlations and cumulants are then evaluated as:

$$\langle\{4\}_{n,m}\rangle_{a,b|c,d} = \left\langle e^{in(\phi_1^a - \phi_2^c) + im(\phi_3^b - \phi_4^d)} \right\rangle \ , \tag{9}$$

$$\mathrm{sc}_{n,m}^{a,b|c,d}\{4\} = \langle\langle\{4\}_{n,m}\rangle\rangle_{a,b|c,d} - \langle\langle\{2\}_n\rangle\rangle_{a|c} \langle\langle\{2\}_m\rangle\rangle_{b|d} \ . \tag{10}$$

The four-subevent method should further suppress the residual non-flow contributions, for instance when each of the two jets from the dijet falls across the boundary between two neighbouring subevents. To maximize the statistical precision, the η ranges for the four subevents are swapped with each other, and the results are averaged to obtain the final values.

5.3 Normalized cumulants

Although the symmetric cumulant $\mathrm{sc}_{n,m}\{4\}$ reflects the nature of the correlation between v_n and v_m, the magnitude of the $\mathrm{sc}_{n,m}\{4\}$ also depends on the square of single flow harmonics v_n^2 and v_m^2, see Eq. (4). The dependence on the single flow harmonics can be scaled out via the normalized cumulants [34, 35]:

$$\mathrm{nsc}_{2,3}\{4\} = \frac{\mathrm{sc}_{2,3}\{4\}}{v_2\{2\}^2 v_3\{2\}^2} = \frac{\langle v_2^2 v_3^2\rangle}{\langle v_2^2\rangle\langle v_3^2\rangle} - 1\,, \tag{11}$$

$$\mathrm{nsc}_{2,4}\{4\} = \frac{\mathrm{sc}_{2,4}\{4\}}{v_2\{2\}^2 v_4\{2\}^2} = \frac{\langle v_2^2 v_4^2\rangle}{\langle v_2^2\rangle\langle v_4^2\rangle} - 1\,, \tag{12}$$

$$\mathrm{nac}_2\{3\} = \frac{\mathrm{ac}_2\{3\}}{v_2\{2\}^2\sqrt{v_4\{2\}^2}} = \frac{\langle v_2^2 v_4 \cos 4(\Phi_2 - \Phi_4)\rangle}{\langle v_2^2\rangle\sqrt{\langle v_4^2\rangle}}\,, \tag{13}$$

where the $v_n\{2\}^2 = \langle v_n^2\rangle$ are flow harmonics obtained using a two-particle correlation method based on a peripheral subtraction technique [7, 14]. In this method, the non-flow effects due to dijets are estimated in this analysis using low-multiplicity events and then subtracted via a "template fit" procedure [7, 14].

6 Analysis procedure

The measurement of the $\mathrm{sc}_{n,m}\{4\}$ and $\mathrm{ac}_2\{3\}$ follows the same analysis procedure as for the four-particle cumulants $c_n\{4\}$ in Ref. [18]. The multi-particle cumulants are calculated in three steps using charged particles with $|\eta| < 2.5$. In the first step, $\langle\{2\}_n\rangle$, $\langle\{3\}_n\rangle$ and $\langle\{4\}_{n,m}\rangle$ from Eqs. (1), (5), (7) and (9) are calculated for each event from particles in one of two different p_T ranges, $0.3 < p_\mathrm{T} < 3$ GeV and $0.5 < p_\mathrm{T} < 5$ GeV. The number of reconstructed charged particles in these p_T ranges are denoted as $N_\mathrm{ch}^\mathrm{sel1}$ and $N_\mathrm{ch}^\mathrm{sel2}$, respectively.

In the second step, the correlators $\langle\{k\}\rangle$ for $0.3 < p_\mathrm{T} < 3$ GeV ($0.5 < p_\mathrm{T} < 5$ GeV) are averaged over events with the same $N_\mathrm{ch}^\mathrm{sel1}$ ($N_\mathrm{ch}^\mathrm{sel2}$) to obtain $\langle\langle\{k\}\rangle\rangle$, and then $\mathrm{sc}_{2,3}\{4\}$, $\mathrm{sc}_{2,4}\{4\}$ and $\mathrm{ac}_2\{3\}$. The $\mathrm{sc}_{2,3}\{4\}$, $\mathrm{sc}_{2,4}\{4\}$ and $\mathrm{ac}_2\{3\}$ values are then combined in broader multiplicity ranges of the event ensemble to obtain statistically significant results.

In the third step, the $\mathrm{sc}_{2,3}\{4\}$, $\mathrm{sc}_{2,4}\{4\}$ and $\mathrm{ac}_2\{3\}$ values obtained for a given $N_\mathrm{ch}^\mathrm{sel1}$ or $N_\mathrm{ch}^\mathrm{sel2}$ are mapped to $\langle N_\mathrm{ch}^\mathrm{rec}\rangle$, the average number of reconstructed charged particles with $p_\mathrm{T} > 0.4$ GeV. The mapping procedure is necessary so that $\mathrm{sc}_{2,3}\{4\}$, $\mathrm{sc}_{2,4}\{4\}$ and $\mathrm{ac}_2\{3\}$ obtained for the two different p_T ranges can be compared using a common x-axis defined by $\langle N_\mathrm{ch}^\mathrm{rec}\rangle$. The $\langle N_\mathrm{ch}^\mathrm{rec}\rangle$ value is then converted to $\langle N_\mathrm{ch}\rangle$, the efficiency-corrected average number of charged particles with $p_\mathrm{T} > 0.4$ GeV, as discussed in Section 4.

In order to account for detector inefficiencies and non-uniformity, particle weights used in Eq. (3) are defined as:

$$w_i(\phi,\eta,p_\mathrm{T}) = d(\phi,\eta)/\epsilon(\eta,p_\mathrm{T})\,. \tag{14}$$

The additional weight factor $d(\phi,\eta)$ accounts for non-uniformities in the azimuthal acceptance of the detector as a function of η. All reconstructed charged particles with $p_\mathrm{T} > 0.3$ GeV are filled into a two-dimensional histogram $N(\phi,\eta)$, and the weight factor is then obtained as $d(\phi,\eta) \equiv \langle N(\eta)\rangle / N(\phi,\eta)$,

where $\langle N(\eta)\rangle$ is the track density averaged over ϕ in the given η bin. This procedure removes most of ϕ-dependent non-uniformity from track reconstruction [17].

In order to calculate the normalized cumulants Eqs. (11)–(13), the flow harmonics $v_n\{2\}$ are obtained from a "template fit" of two-particle $\Delta\phi$ correlation as described in Refs. [7, 14]. The $v_n\{2\}$ values are calculated identically as in the previous ATLAS publications [7, 14], but are further corrected for a bias, which exists only if $v_n\{2\}$ changes with $N_{\rm ch}^{\rm rec}$. The details of the correction procedure are given in the Appendix A and are discussed briefly below.

The standard procedure of Refs. [7, 14] first constructs a $\Delta\phi$ distribution for pairs with $|\Delta\eta| > 2$, so called per-trigger-particle yield, $Y(\Delta\phi)$ for a given $N_{\rm ch}^{\rm rec}$ range. The dominating non-flow jet peak at $\Delta\phi \sim \pi$ is estimated using low-multiplicity events with $N_{\rm ch}^{\rm rec} < 20$ and separated via a template fit procedure, and the harmonic modulation of the remaining component is taken as the $v_n\{2\}^2$ [7]:

$$Y(\Delta\phi) = F\,Y(\Delta\phi)^{\rm peri} + G^{\rm tmp}\left(1 + 2\sum_{n=2}^{\infty} v_n\{2,{\rm tmp}\}^2\cos n\Delta\phi\right), \tag{15}$$

where superscripts "peri" and "tmp" indicate quantities for the $N_{\rm ch}^{\rm rec} < 20$ event class and quantities after the template fit for the event class of interest, respectively. The scale factor F and pedestal $G^{\rm tmp}$ are fixed by the fit, and $v_n\{2,{\rm tmp}\}$ are calculated from a Fourier transform. This procedure implicitly assumes that $v_n\{2\}$ is independent of $N_{\rm ch}^{\rm rec}$, and results in a small bias if $v_n\{2\}$ does change with $N_{\rm ch}^{\rm rec}$:

$$v_n\{2\}^2 = v_n\{2,{\rm tmp}\}^2 - \frac{F\,G^{\rm peri}}{G^{\rm cent}}\left(v_n\{2,{\rm tmp}\}^2 - v_n\{2,{\rm peri}\}^2\right), \tag{16}$$

where $G^{\rm cent}$ and $G^{\rm peri}$ are the pedestals for $Y(\Delta\phi)$ and $Y(\Delta\phi)^{\rm peri}$, respectively, and $v_n\{2,{\rm peri}\}$ is the true flow harmonic for $N_{\rm ch}^{\rm rec} < 20$. Since $v_n\{2,{\rm peri}\}$ is unknown, the correction is applied starting from the third $N_{\rm ch}^{\rm rec}$ bin, by using $v_n\{2,{\rm tmp}\}$ of the second $N_{\rm ch}^{\rm rec}$ bin as an estimate of the true flow harmonics. In p+Pb and Pb+Pb collisions, this correction in the $N_{\rm ch}^{\rm rec} > 100$ region amounts to a 2–6% reduction for $v_2\{2,{\rm tmp}\}$ and a 4–9% reduction for $v_3\{2,{\rm tmp}\}$ and $v_4\{2,{\rm tmp}\}$. The correction is smaller for $v_2\{2,{\rm tmp}\}$ in pp collisions as it is nearly independent of $N_{\rm ch}^{\rm rec}$ [7].

7 Systematic uncertainties

The evaluation of the systematic uncertainties follows closely the procedure established for the four-particle cumulants $c_n\{4\}$ measured in Ref. [18]. The main sources of systematic uncertainties are related to the detector azimuthal non-uniformity, track selection, track reconstruction efficiency, trigger efficiency and pileup. Due to the relatively poor statistics and larger non-flow effects, the systematic uncertainties are typically larger in pp collisions. The systematic uncertainties are also generally larger for four-particle cumulants ${\rm sc}_{n,m}\{4\}$ than the three-particle cumulants ${\rm ac}_2\{3\}$, since the $|{\rm sc}_{n,m}\{4\}|$ values are much smaller than those for ${\rm ac}_2\{3\}$. The systematic uncertainties are generally similar among the two- and three- and four-subevent methods, but are different from those for the standard method, which has strong influence from non-flow correlations. The following discussion focuses on the three-subevent method, which is the default method used to present the final results.

The effect of detector azimuthal non-uniformity is accounted for using the weight factor $d(\phi,\eta)$. The impact of the reweighting procedure is studied by fixing the weight to unity and repeating the analysis. The results are mostly consistent with the nominal results. The corresponding uncertainties for ${\rm sc}_{n,m}\{4\}$

are 0–4%, 0–2% and 1–2% in pp, p+Pb and Pb+Pb collisions, respectively. The uncertainties for $\mathrm{ac}_2\{3\}$ are 0–2% in pp collisions, and 0–1% in p+Pb and Pb+Pb collisions.

The systematic uncertainty associated with the track selection is estimated by tightening the $|d_0|$ and $|z_0 \sin\theta|$ requirements. They are varied from default requirement of less than 1.5 mm to less than 1 mm. In p+Pb and Pb+Pb collisions, the requirement on the significance of impact parameters, $|d_0|/\sigma_{d_0}$ and $|z_0 \sin\theta|/\sigma_{z_0}$ are also varied from less than 3 to less than 2. For each variation, the tracking efficiency is re-evaluated and the analysis is repeated. For $\mathrm{ac}_2\{3\}$, which has a large flow signal, the differences from the nominal results are observed to be less than 2% for all systems. For $\mathrm{sc}_{n,m}\{4\}$, whose signal is small, the differences from the nominal results are found to be in the range of 2–10% in pp collisions, 2–7% in p+Pb collisions and 2–4% in Pb+Pb collisions. The differences are smaller for results obtained for $0.5 < p_{\mathrm{T}} < 5$ GeV than those obtained for $0.3 < p_{\mathrm{T}} < 3$ GeV.

Previous measurements indicate that the azimuthal correlations (both the flow and non-flow components) have a strong dependence on p_{T}, but a relatively weak dependence on η [5, 7]. Therefore, p_{T}-dependent systematic effects in the track reconstruction efficiency could affect the cumulant values. The uncertainty in the track reconstruction efficiency is mainly due to differences in the detector conditions and material description between the simulation and the data. The efficiency uncertainty varies between 1% and 4%, depending on track η and p_{T} [7, 17]. Its impact on multi-particle cumulants is evaluated by repeating the analysis with the tracking efficiency varied up and down by its corresponding uncertainty as a function of track p_{T}. For the standard cumulant method, which is more sensitive to jets and dijets, the evaluated uncertainty amounts to 2–6% in pp collisions and less than 2% in p+Pb collisions for $\langle N_{\mathrm{ch}} \rangle > 100$. For the subevent methods, the evaluated uncertainty is typically less than 3% for most of the $\langle N_{\mathrm{ch}} \rangle$ ranges.

Most events in pp and p+Pb collisions are collected with the HMT triggers with several $N_{\mathrm{ch}}^{\mathrm{rec}}$ thresholds. In order to estimate the possible bias due to trigger inefficiency as a function of $\langle N_{\mathrm{ch}} \rangle$, the offline $N_{\mathrm{ch}}^{\mathrm{rec}}$ requirements are changed such that the HMT trigger efficiency is at least 50% or 80%. The results are obtained independently for each variation. These results are found to be consistent with each other for the subevent methods, and show some differences for the standard cumulant method in the low $\langle N_{\mathrm{ch}} \rangle$ region. The nominal analysis is performed using the 50% efficiency selection and the differences between the nominal results and those from the 80% efficiency selection are included in the systematic uncertainty. The changes for pp collisions are in the range of 5–15% for $\mathrm{sc}_{2,3}\{4\}$, 2–8% for $\mathrm{sc}_{2,4}\{4\}$ and 1–5% for $\mathrm{ac}_2\{3\}$, respectively. The ranges for p+Pb collisions are much smaller due to much sharper turn on of the trigger efficiency and larger signal, they are estimated to be 1–3% for $\mathrm{sc}_{2,3}\{4\}$, 2–4% for $\mathrm{sc}_{2,4}\{4\}$ and 1–2% for $\mathrm{ac}_2\{3\}$, respectively.

In this analysis, a pileup rejection criterion is applied to reject events containing additional vertices in pp and p+Pb collisions. In order to check the impact of residual pileup, the analysis is repeated without the pileup rejection criterion. No differences are observed in p+Pb collisions, as is expected since the μ values in p+Pb are modest. For the 13 TeV pp dataset, the differences with and without pileup rejection are in the range of 0–7% for $\mathrm{sc}_{2,3}\{4\}$, 2–15% for $\mathrm{sc}_{2,4}\{4\}$ and 2–3% for $\mathrm{ac}_2\{3\}$ respectively. As a cross check, the pp data are divided into two samples based on the μ value: $\mu > 0.4$ and $\mu < 0.4$, and the results are compared. No systematic differences are observed between the two independent datasets.

The systematic uncertainties from different sources are added in quadrature to determine the total systematic uncertainty. In p+Pb and Pb+Pb collisions, the total uncertainties are in the range of 3–8% for $\mathrm{sc}_{2,3}\{4\}$, 1–5% for $\mathrm{sc}_{2,4}\{4\}$ and 1–4% for $\mathrm{ac}_2\{3\}$. In pp collisions, the total uncertainties are larger, mainly due to larger non-flow, larger pileup and poorer turn on for the HMT triggers. They are in the ranges of 10–20%

for $\mathrm{sc}_{2,3}\{4\}$, 10–20% for $\mathrm{sc}_{2,4}\{4\}$ and 2–5% for $\mathrm{ac}_2\{3\}$, respectively. The total systematic uncertainties are generally smaller than the statistical uncertainties.

The $v_n\{2\}$ values used to obtain normalized cumulants are measured following the same prescription of the previous ATLAS publications [7,14], resulting in very similar systematic uncertainties. The correction for the bias of the template fit procedure, as described in Section 6, reduces the sensitivity on the choice of the peripheral $N_{\mathrm{ch}}^{\mathrm{rec}}$ bin. The uncertainties of normalized cumulants are obtained by propagation of the uncertainties from the original cumulants and $v_n\{2\}$, after accounting for the partial cancellation of the correlated systematic uncertainties.

8 Results

The results are presented in two parts. Section 8.1 presents a detailed comparison between the standard method and subevent methods to demonstrate the ability of the subevent methods to suppress non-flow correlations. Section 8.2 compares the cumulants among pp, p+Pb and Pb+Pb collisions to provide insight on the common nature of collectivity in these systems.

8.1 Comparison between standard and subevent methods

The top row of Figure 1 compares the $\mathrm{sc}_{2,3}\{4\}$ obtained from the standard, two-, three- and four-subevent methods from pp collisions in $0.3 < p_{\mathrm{T}} < 3$ GeV (left panel) and $0.5 < p_{\mathrm{T}} < 5$ GeV (right panel). The values from the standard method are positive over the full $\langle N_{\mathrm{ch}} \rangle$ range, and are larger at lower $\langle N_{\mathrm{ch}} \rangle$ or at higher p_{T}. These behaviors suggest that the $\mathrm{sc}_{2,3}\{4\}$ values from the standard method in pp collisions, including those from Ref. [19], are strongly influenced by non-flow effects in all $\langle N_{\mathrm{ch}} \rangle$ and p_{T} ranges. In contrast, the values from the subevent methods are negative over the full $\langle N_{\mathrm{ch}} \rangle$ range, and they are slightly more negative at lowest $\langle N_{\mathrm{ch}} \rangle$ and also more negative at higher p_{T}. The results are consistent among various subevent methods for $0.3 < p_{\mathrm{T}} < 3$ GeV. For the high p_{T} region of $0.5 < p_{\mathrm{T}} < 5$ GeV, results from the two-subevent method are systematically lower than the three- and four-subevent methods, suggesting that the two-subevent method may be affected by negative non-flow contributions. Such negative non-flow correlation has been observed in a PYTHIA8 calculation [16].

The middle row of Figure 1 shows the $\mathrm{sc}_{2,3}\{4\}$ from p+Pb collisions. At $\langle N_{\mathrm{ch}} \rangle > 140$, the values are negative and consistent among all four methods, reflecting genuine long-range collective correlations. At $\langle N_{\mathrm{ch}} \rangle < 140$, the values are different between the standard method and the subevent methods. The $\mathrm{sc}_{2,3}\{4\}$ from the standard method changes sign around $\langle N_{\mathrm{ch}} \rangle \sim 80$ and remains positive at lower $\langle N_{\mathrm{ch}} \rangle$, reflecting the contribution from non-flow correlations. In contrast, the $\mathrm{sc}_{2,3}\{4\}$ from various subevent methods are negative and consistent with each other at $\langle N_{\mathrm{ch}} \rangle < 140$, suggesting that they mainly reflect the genuine long-range correlations.

The bottom row of Figure 1 shows the $\mathrm{sc}_{2,3}\{4\}$ from Pb+Pb collisions. The results are consistent among all four methods across most of the $\langle N_{\mathrm{ch}} \rangle$ range, although the results from the standard method are systematically larger. In the low $\langle N_{\mathrm{ch}} \rangle$ region, where the non-flow is expected to be significant, the uncertainties of the results are too large to distinguish between different methods.

The results for symmetric cumulant $\mathrm{sc}_{2,4}\{4\}$ are presented in Figure 2. The top row shows the $\mathrm{sc}_{2,4}\{4\}$ obtained from the standard, two-subevent, three-subevent and four-subevent methods from pp collisions

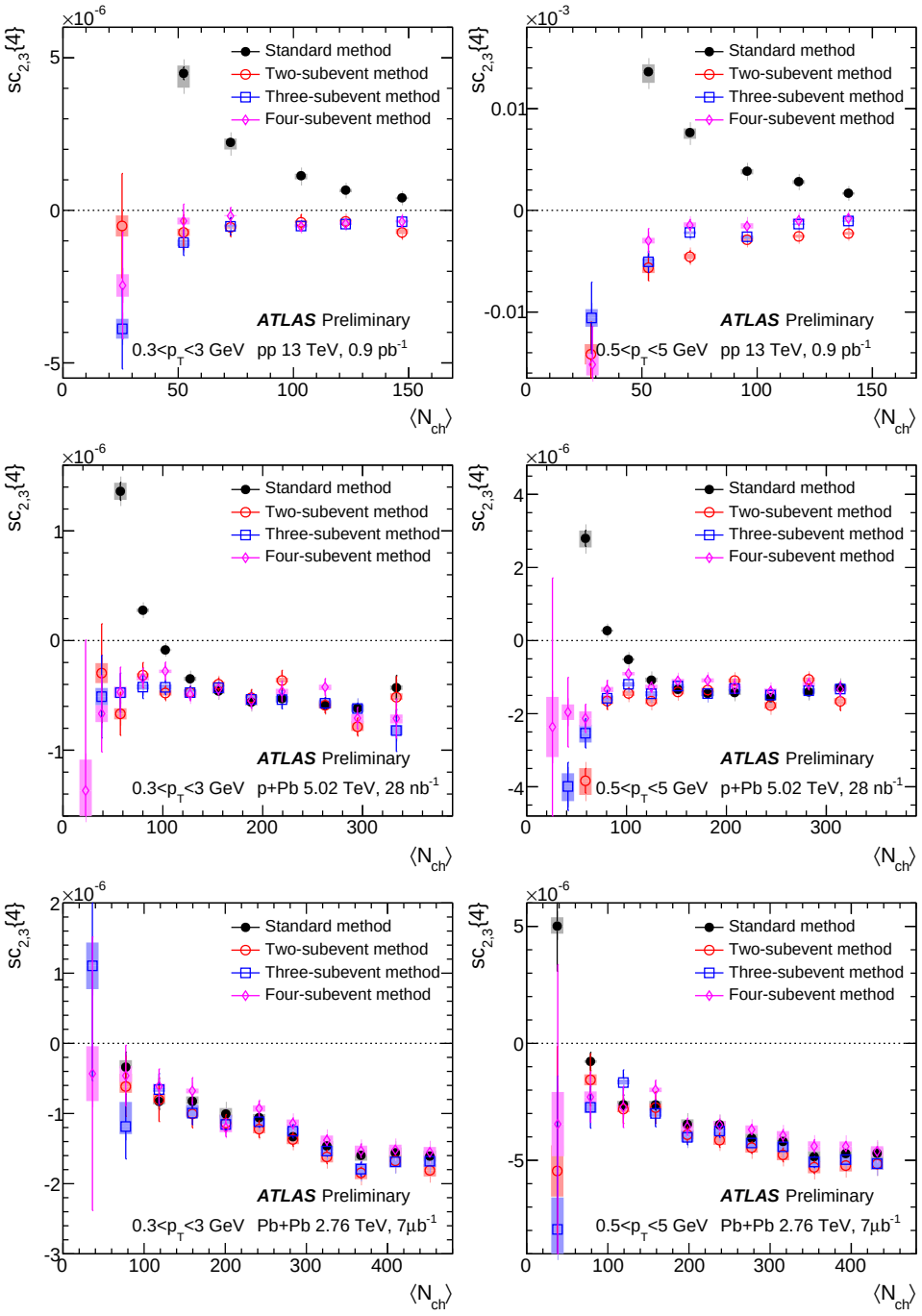

Figure 1: . The symmetric cumulant $\mathrm{sc}_{2,3}\{4\}$ as a function of $\langle N_{\mathrm{ch}} \rangle$ for $0.3 < p_{\mathrm{T}} < 3$ GeV (left panels) and $0.5 < p_{\mathrm{T}} < 5$ GeV (right panels) obtained for pp collisions (top row), p+Pb collisions (middle row) and low-multiplicity Pb+Pb collisions (bottom row). In each panel, the $\mathrm{sc}_{2,3}\{4\}$ is obtained from the standard method (filled symbol), the two-subevent method (open circles), three-subevent method (open squares) and four-subevent method (open diamonds). The error bars and shaded boxes represent the statistical and systematic uncertainties, respectively.

in $0.3 < p_{\mathrm{T}} < 3$ GeV (left panel) and $0.5 < p_{\mathrm{T}} < 5$ GeV (right panel). The values of $\mathrm{sc}_{2,4}\{4\}$ are positive for all four methods. However, the results from the standard method are much larger than the subevent methods and also exhibit a much stronger increase towards the lower $\langle N_{\mathrm{ch}} \rangle$ region. This behavior is consistent with the expectation that the standard method is more affected by dijets. Significant differences are also observed between the two-subevent and three- or four-subevent methods at low $\langle N_{\mathrm{ch}} \rangle$, but these differences decrease and disappear for $\langle N_{\mathrm{ch}} \rangle > 100$. Within the statistical uncertainties of the measurement, no differences are observed between the three- and four-subevent methods. This comparison suggests that the two-subevent method may not be sufficient to reject non-flow from dijets in pp collisions, and methods with three or more subevents are required to suppress the non-flow correlations over the measured $\langle N_{\mathrm{ch}} \rangle$ range.

The middle row of Figure 2 shows $\mathrm{sc}_{2,4}\{4\}$ from p+Pb collisions. Significant differences are observed between the standard method and the subevent methods over the full $\langle N_{\mathrm{ch}} \rangle$ range. However, no differences are observed among various subevent methods. These results suggest that the standard method is contaminated by large contributions from non-flow correlations at low $\langle N_{\mathrm{ch}} \rangle$, and this contribution may not vanish even at large $\langle N_{\mathrm{ch}} \rangle$ values. All subevent methods suggest an increase of $\mathrm{sc}_{2,4}\{4\}$ toward lower $\langle N_{\mathrm{ch}} \rangle$ for $\langle N_{\mathrm{ch}} \rangle < 40$, which may reflect some residual non-flow correlations in this region.

The bottom row of Figure 2 shows $\mathrm{sc}_{2,4}\{4\}$ from Pb+Pb collisions. The $\mathrm{sc}_{2,4}\{4\}$ values increase gradually with $\langle N_{\mathrm{ch}} \rangle$ for all four methods. This increase reflects the known fact that the v_2 increases with $\langle N_{\mathrm{ch}} \rangle$ in Pb+Pb collisions [36]. The values from the standard method are systematically larger than those from the subevent methods, and this difference varies slowly with $\langle N_{\mathrm{ch}} \rangle$, similar to the behavior observed for the p+Pb collisions in the large $\langle N_{\mathrm{ch}} \rangle$ region.

The results for asymmetric cumulant $\mathrm{ac}_2\{3\}$ are presented in Figure 3. The top row shows the results obtained from the standard, two-subevent, and three-subevent methods from pp collisions in $0.3 < p_{\mathrm{T}} < 3$ GeV (left panel) and $0.5 < p_{\mathrm{T}} < 5$ GeV (right panel). The results are positive for all methods. The results from the standard method are much larger than those from the subevent methods, consistent with the expectation that the standard method is more affected by non-flow correlations from dijets. Significant differences are also observed between the two-subevent and three-subevent methods at low $\langle N_{\mathrm{ch}} \rangle$, but these differences decrease and disappear at $\langle N_{\mathrm{ch}} \rangle > 100$. The $\mathrm{ac}_2\{3\}$ values from the three-subevent method show a slight increase for $\langle N_{\mathrm{ch}} \rangle < 40$ but are nearly constant for $\langle N_{\mathrm{ch}} \rangle > 40$. This behavior suggests that in the three-subevent method, the non-flow contribution may play some role at $\langle N_{\mathrm{ch}} \rangle < 40$, but is negligible for $\langle N_{\mathrm{ch}} \rangle > 40$. Therefore, the $\mathrm{ac}_2\{3\}$ from the three-subevent method supports the existence of a three-particle long-range collective flow that is nearly $\langle N_{\mathrm{ch}} \rangle$-independent in pp collisions, consistent with the $\langle N_{\mathrm{ch}} \rangle$-independent behavior of v_2 and v_4 previously observed from the two-particle correlation analysis [7].

The middle and bottom rows of Figure 3 show $\mathrm{ac}_2\{3\}$ from p+Pb and Pb+Pb collisions, respectively. The $\mathrm{ac}_2\{3\}$ values from the standard method have a significant non-flow contribution up to $\langle N_{\mathrm{ch}} \rangle \sim 200$ in p+Pb collisions and $\langle N_{\mathrm{ch}} \rangle \sim 80$ in Pb+Pb collisions. In the subevent methods, the influence of non-flow contributions is very small for $\langle N_{\mathrm{ch}} \rangle > 60$ in both collision systems, and therefore the $\langle N_{\mathrm{ch}} \rangle$ dependence of $\mathrm{ac}_2\{3\}$ reflects the $\langle N_{\mathrm{ch}} \rangle$ dependence of the v_2 and v_4. The $\mathrm{ac}_2\{3\}$ values from the subevent methods increase with $\langle N_{\mathrm{ch}} \rangle$, and the increase is stronger in Pb+Pb collisions. This is consistent with previous observations that v_2 and v_4 increase with $\langle N_{\mathrm{ch}} \rangle$ more strongly in Pb+Pb than in p+Pb collisions [17].

The values of $\mathrm{sc}_{2,4}\{4\}$ and $\mathrm{ac}_2\{3\}$, both measures of correlations between v_2 and v_4, show significant differences between the standard method and subevent methods (as shown in Figures 2 and 3). The $\langle N_{\mathrm{ch}} \rangle$ dependence of these differences decreases gradually with $\langle N_{\mathrm{ch}} \rangle$, and is consistent with influence of

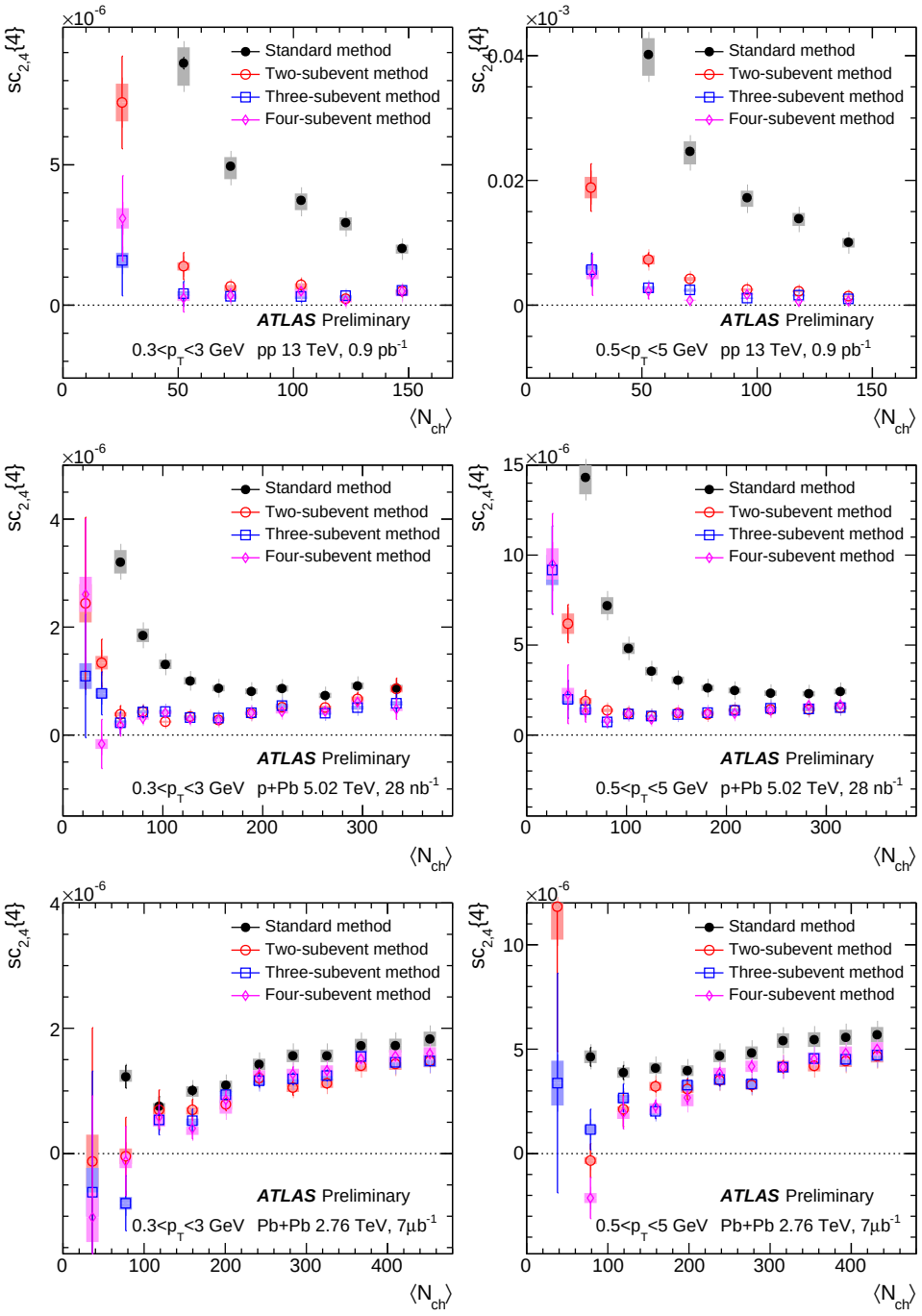

Figure 2: The symmetric cumulant $\mathrm{sc}_{2,4}\{4\}$ as a function of $\langle N_{\mathrm{ch}} \rangle$ for $0.3 < p_{\mathrm{T}} < 3$ GeV (left panels) and $0.5 < p_{\mathrm{T}} < 5$ GeV (right panels) obtained for pp collisions (top row), p+Pb collisions (middle row) and low-multiplicity Pb+Pb collisions (bottom row). In each panel, the $\mathrm{sc}_{2,4}\{4\}$ is obtained from the standard method (filled symbol), two-subevent method (open circles), three-subevent method (open squares) and four-subevent method (open diamonds). The error bars and shaded boxes represent the statistical and systematic uncertainties, respectively.

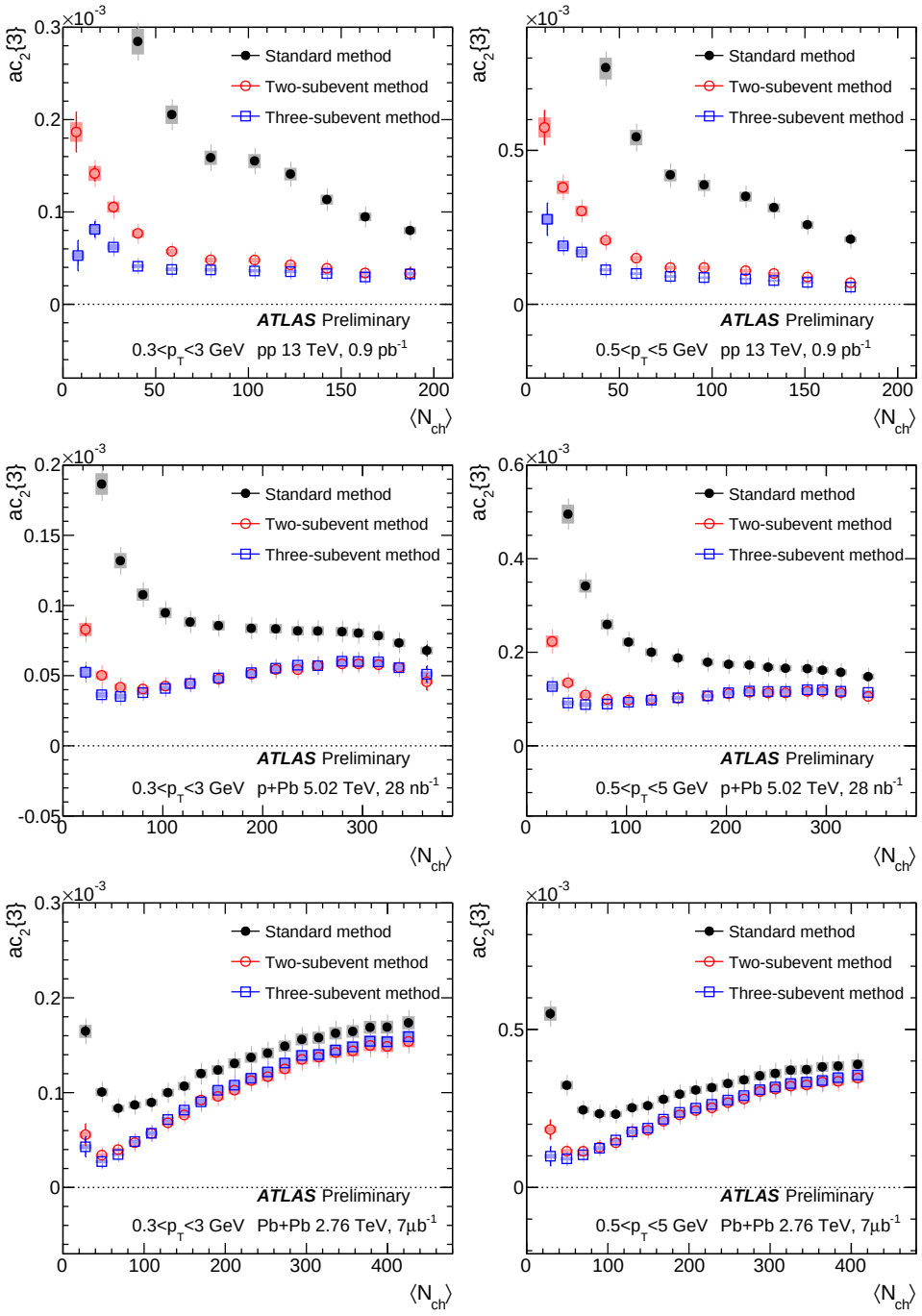

Figure 3: The asymmetric cumulant $\mathrm{ac}_2\{3\}$ as a function of $\langle N_{\mathrm{ch}} \rangle$ for $0.3 < p_{\mathrm{T}} < 3$ GeV (left panels) and $0.5 < p_{\mathrm{T}} < 5$ GeV (right panels) obtained for pp collisions (top row), p+Pb collisions (middle row) and low-multiplicity Pb+Pb collisions (bottom row). In each panel, the $\mathrm{ac}_2\{3\}$ is obtained from the standard method (filled symbol), two-subevent method (open circles), and three-subevent method (open squares). The error bars and shaded boxes represent the statistical and systematic uncertainties, respectively.

non-flow which is expected to scale as $1/\langle N_{\rm ch}\rangle$. However, these differences seem to persist for $\langle N_{\rm ch}\rangle > 200$ in p+Pb collisions and for $\langle N_{\rm ch}\rangle > 150$ in Pb+Pb collisions, incompatible with the predicted behavior of non-flow. The differences at large $\langle N_{\rm ch}\rangle$ may arise from longitudinal flow decorrelations [37, 38], which have been measured by CMS [39] and ATLAS [40]. Decorrelation effects are found to be large for v_4 and strongly correlated with v_2, and therefore they are expected to reduce the $\mathrm{sc}_{2,4}\{4\}$ and $\mathrm{ac}_2\{3\}$ in the subevent method. Therefore, the observed differences between the standard method and subevent method reflect the combined contribution from non-flow which dominates at the low $\langle N_{\rm ch}\rangle$ region, and decorrelation which is more important at large $\langle N_{\rm ch}\rangle$.

The results presented above suggest that the three-subevent method is sufficient to suppress most of the non-flow effects. It is therefore used as the default method for the discussion below.

8.2 Comparison between collision systems

Figure 4 shows a direct comparison of cumulants for the three collision systems. The three panels in the top row show the results for $\mathrm{sc}_{2,3}\{4\}$, $\mathrm{sc}_{2,4}\{4\}$ and $\mathrm{ac}_2\{3\}$, respectively, for $0.3 < p_{\rm T} < 3$ GeV. These results support an anti-correlation between v_2 and v_3 and a positive correlation between v_2 and v_4. Such correlation patterns have previously been observed in large collision systems [41–43], but are now confirmed also in the small collision systems without the influence of non-flow effects. In the multiplicity range covered by the pp collisions, $\langle N_{\rm ch}\rangle < 150$, the results for symmetric cumulants $\mathrm{sc}_{2,3}\{4\}$ and $\mathrm{sc}_{2,4}\{4\}$ are similar among the three systems. In the range $\langle N_{\rm ch}\rangle > 150$, $\mathrm{sc}_{2,3}\{4\}$ and $\mathrm{sc}_{2,4}\{4\}$ are larger in Pb+Pb than in p+Pb collisions. The results for $\mathrm{ac}_2\{3\}$ are similar among the three systems at $\langle N_{\rm ch}\rangle < 100$, but they deviate from each other at higher $\langle N_{\rm ch}\rangle$. The pp data are approximately constant or decrease slightly with $\langle N_{\rm ch}\rangle$, while the p+Pb and Pb+Pb data show significant increases as a function of $\langle N_{\rm ch}\rangle$. The bottom row shows the results for the higher $p_{\rm T}$ range $0.5 < p_{\rm T} < 5$ GeV, where similar trends are observed.

Figure 5 shows the results for normalized cumulants, $\mathrm{nsc}_{2,3}\{4\}$, $\mathrm{nsc}_{2,4}\{4\}$ and $\mathrm{nac}_2\{3\}$, compared among the three systems. The normalized cumulants generally show a much weaker $\langle N_{\rm ch}\rangle$ dependence at $\langle N_{\rm ch}\rangle > 100$, where the statistical uncertainties are small. This behavior implies that the strong $\langle N_{\rm ch}\rangle$ dependence of the $\mathrm{sc}_{n,m}\{4\}$ and $\mathrm{ac}_2\{3\}$ values reflects the $\langle N_{\rm ch}\rangle$ dependence of the v_n values, and these dependencies are removed in the normalized cumulants. The normalized cumulants are also similar among different collision systems at large $\langle N_{\rm ch}\rangle$, although some differences at the relative level of 20–30% are observed for smaller $\langle N_{\rm ch}\rangle$. The only exception is $\mathrm{nsc}_{2,3}\{4\}$, whose values in the pp collisions are very different from those in p+Pb and Pb+Pb collisions. In contrast, the $\mathrm{sc}_{2,3}\{4\}$ values in Figure 4 show good consistency among different systems. This suggests that the $\langle v_3^2\rangle$ values from the template fit method [7] may be significantly underestimated. As pointed out in Ref. [7] and emphasized in Appendix A, the template fit method, and other methods based on peripheral subtraction in general [5, 15], tend to underestimate the odd flow harmonics, due to the presence of a large away-side peak at $\Delta\phi \sim \pi$ in the two-particle correlation function. The comparison of $\mathrm{sc}_{2,3}\{4\}$ and $\mathrm{nsc}_{2,3}\{4\}$ among different collision systems provides indirect evidence for this underestimation of $\langle v_3^2\rangle$.

Figure 5 shows that the normalized cumulants are consistent between $0.3 < p_{\rm T} < 3$ GeV and $0.5 < p_{\rm T} < 5$ GeV. On the other hand, the magnitudes of the cumulants in Figure 4 differ by a large factor between the two $p_{\rm T}$ ranges: about a factor of three for $\mathrm{sc}_{2,3}\{4\}$ and $\mathrm{sc}_{2,4}\{4\}$, and a factor of two for $\mathrm{ac}_2\{3\}$. These results suggest that the $p_{\rm T}$ dependence of $\mathrm{sc}_{2,3}\{4\}$, $\mathrm{sc}_{2,4}\{4\}$ and $\mathrm{ac}_2\{3\}$ largely reflects the $p_{\rm T}$ dependence of the v_n at the single-particle level.

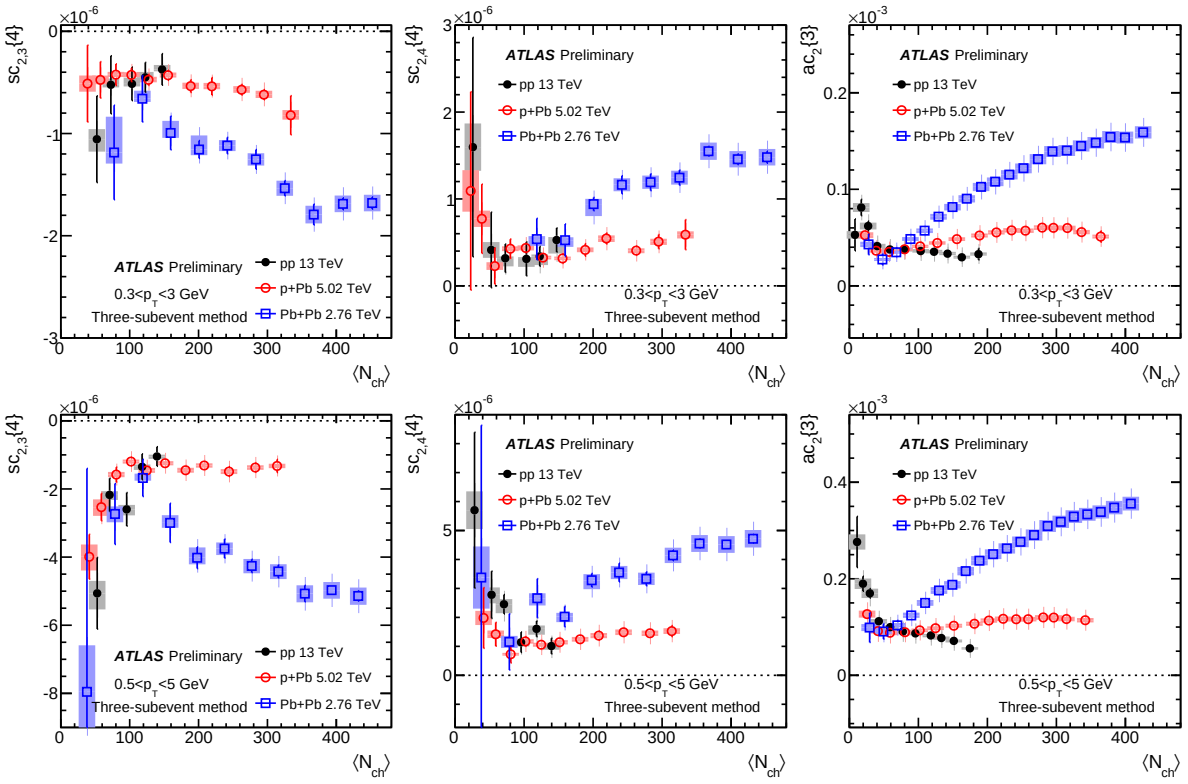

Figure 4: The $\langle N_{\mathrm{ch}} \rangle$ dependence of $\mathrm{sc}_{2,3}\{4\}$ (left panels), $\mathrm{sc}_{2,4}\{4\}$ (middle panels) and $\mathrm{ac}_2\{3\}$ (right panels) in $0.3 < p_{\mathrm{T}} < 3$ GeV (top row) and $0.5 < p_{\mathrm{T}} < 5$ GeV (bottom row) obtained for pp collisions (solid circles), p+Pb collisions (open circles) and low-multiplicity Pb+Pb collisions (open squares). The error bars and shaded boxes represent the statistical and systematic uncertainties, respectively.

9 Discussion and summary

Three- and four-particle cumulants involving correlations between two harmonics of different order v_n and v_m are measured in $\sqrt{s}$ = 13 TeV pp, $\sqrt{s_{\mathrm{NN}}}$ = 5.02 TeV p+Pb, and low-multiplicity $\sqrt{s_{\mathrm{NN}}}$ = 2.76 TeV Pb+Pb collisions with the ATLAS detector at the LHC, with total integrated luminosities of 0.9 pb^{-1}, 28 nb^{-1}, and 7 μb^{-1}, respectively. The correlation between v_n and v_m is studied using four-particle symmetric cumulants $\mathrm{sc}_{2,3}\{4\}$, $\mathrm{sc}_{2,4}\{4\}$ and the three-particle asymmetric cumulant $\mathrm{ac}_2\{3\}$. The symmetric cumulants $\mathrm{sc}_{n,m}\{4\} = \langle v_n^2 v_m^2 \rangle - \langle v_n^2 \rangle \langle v_m^2 \rangle$ probe the correlation of the flow magnitudes, while the asymmetric cumulant $\mathrm{ac}_2\{3\} = \langle v_2^2 v_4 \cos 4(\Phi_2 - \Phi_4) \rangle$ is sensitive to correlations involving both the flow magnitude v_n and flow phase Φ_n. They are calculated using the standard cumulant method, as well as the two-, three- and four-subevent methods to suppress non-flow effects. The final results are presented as a function of the average number of charged particles with $p_{\mathrm{T}} > 0.4$ GeV, $\langle N_{\mathrm{ch}} \rangle$.

Significant differences are observed between the standard method and the subevent methods over the full $\langle N_{\mathrm{ch}} \rangle$ range in pp collisions, as well as over the low $\langle N_{\mathrm{ch}} \rangle$ range in p+Pb and Pb+Pb collisions. The differences are larger for particles at higher p_{T} or at smaller $\langle N_{\mathrm{ch}} \rangle$. When analyzed with the standard method in pp collisions, this behavior is compatible with the dominance of the non-flow correlations rather than the long-range collective flow correlations. Systematic, but much smaller, differences are also

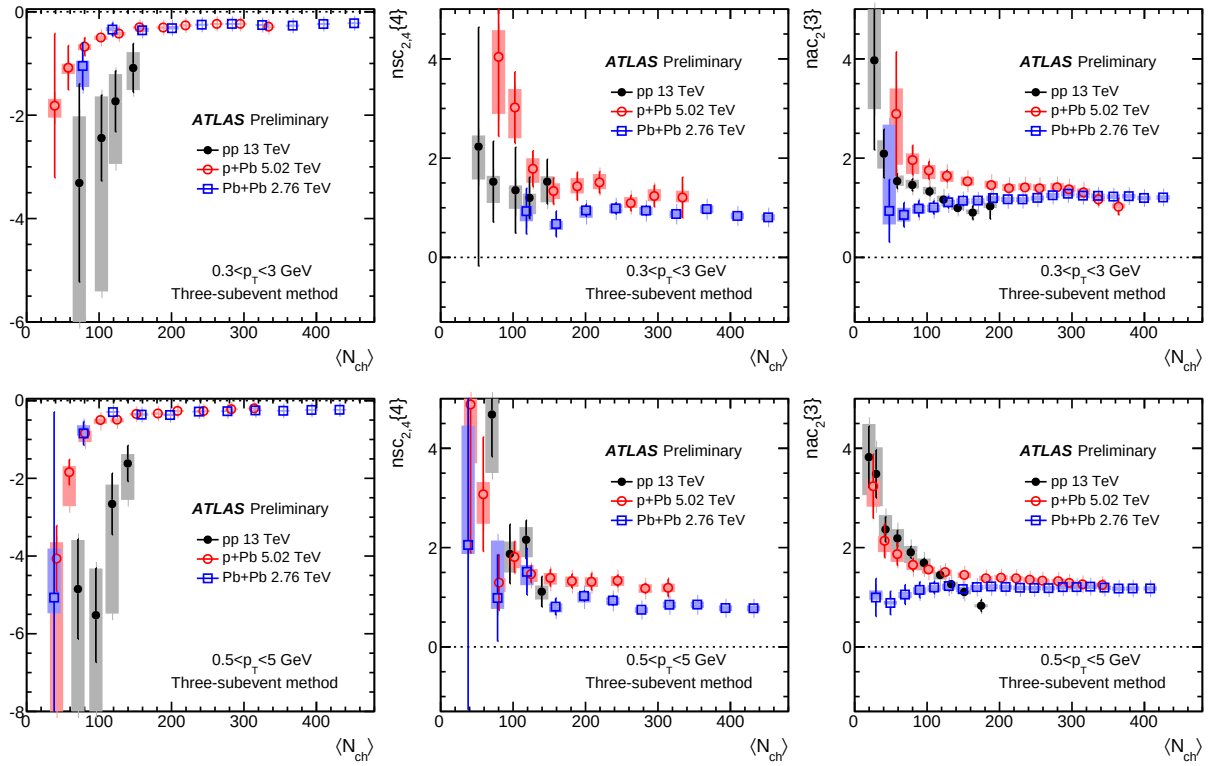

Figure 5: The $\langle N_{\mathrm{ch}} \rangle$ dependence of $\mathrm{nsc}_{2,3}\{4\}$ (left panels), $\mathrm{nsc}_{2,4}\{4\}$ (middle panels) and $\mathrm{nac}_2\{3\}$ (right panels) in $0.3 < p_{\mathrm{T}} < 3$ GeV (top row) and $0.5 < p_{\mathrm{T}} < 5$ GeV (bottom row) obtained for pp collisions (solid circles), p+Pb collisions (open circles) and low-multiplicity Pb+Pb collisions (open squares). The error bars and shaded boxes represent the statistical and systematic uncertainties, respectively.

observed in the low $\langle N_{\mathrm{ch}} \rangle$ region between the two-subevent method and three- or four-subevent methods, which indicates that the two-subevent method may still be affected by correlations arising from jets. On the other hand no differences are observed between the three-subevent and four-subevent methods, within experimental uncertainties, suggesting that methods with three or more subevents are sufficient to reject non-flow correlations from jets. Therefore the three-subevent method is used to present the main results in this analysis.

The three-subevent method provides a measurement of negative $\mathrm{sc}_{2,3}\{4\}$ and positive $\mathrm{sc}_{2,4}\{4\}$ and $\mathrm{ac}_2\{3\}$ over nearly the full $\langle N_{\mathrm{ch}} \rangle$ range and in all three collision systems. These results indicate an anti-correlation between v_2 and v_3 and a positive correlation between v_2 and v_4. Such correlation patterns have previously been observed in large collision systems [41–43], but are now confirmed in small collision systems without the influence of non-flow effects. The values for $\mathrm{sc}_{2,3}\{4\}$ and $\mathrm{sc}_{2,4}\{4\}$ are consistent in pp and p+Pb collisions over the same $\langle N_{\mathrm{ch}} \rangle$ range, but their magnitudes at large $\langle N_{\mathrm{ch}} \rangle$ are much smaller than those for Pb+Pb collisions. The values of $\mathrm{ac}_2\{3\}$ are similar at very low $\langle N_{\mathrm{ch}} \rangle$ among the three systems, but are very different at large $\langle N_{\mathrm{ch}} \rangle$. On the other hand, after scaling by the $\langle v_n^2 \rangle$ estimated from a two-particle analysis [7, 14], the resulting normalized cumulants $\mathrm{nsc}_{2,3}\{4\}$, $\mathrm{nsc}_{2,4}\{4\}$ and $\mathrm{nac}_2\{3\}$ show a much weaker dependence on $\langle N_{\mathrm{ch}} \rangle$, and their values are much closer to each other among the three systems. The magnitudes of the normalized cumulants are also similar to each other for $0.5 < p_{\mathrm{T}} < 5$ GeV as well as $0.3 < p_{\mathrm{T}} < 3$ GeV. This suggests that the $\langle N_{\mathrm{ch}} \rangle$, p_{T} and system dependence of the $\mathrm{sc}_{2,3}\{4\}$, $\mathrm{sc}_{2,4}\{4\}$

and $\mathrm{ac}_2\{3\}$ reflect mostly the $\langle N_{\mathrm{ch}} \rangle$, p_{T} and system dependence of $\langle v_n^2 \rangle$, but the relative strengths of the correlations are similar for the three collision systems.

The new results obtained with the subevent cumulant technique provide further evidence that the ridge is indeed a long-range collective phenomenon involving many particles distributed across a broad rapidity interval. The similarity between different collision systems for $\mathrm{nsc}_{2,3}\{4\}$, $\mathrm{nsc}_{2,4}\{4\}$ and $\mathrm{nac}_2\{3\}$, and the weak dependence of these observables on the p_{T} range and $\langle N_{\mathrm{ch}} \rangle$, largely free from non-flow effects, provide an important input towards understanding the space-time dynamics and the properties of the medium created in small collision systems.

References

[1] E. Shuryak, *Strongly coupled quark-gluon plasma in heavy ion collisions*, Rev. Mod. Phys. **89** (2017) 035001, arXiv:1412.8393 [hep-ph].

[2] CMS Collaboration, *Observation of long-range near-side angular correlations in proton-lead collisions at the LHC*, Phys. Lett. B **718** (2013) 795, arXiv:1210.5482 [nucl-ex].

[3] ALICE Collaboration, *Long-range angular correlations on the near and away side in p-Pb collisions at* $\sqrt{s_{NN}}$ = 5.02 *TeV*, Phys. Lett. B **719** (2013) 29, arXiv:1212.2001 [nucl-ex].

[4] ATLAS Collaboration, *Observation of Associated Near-side and Away-side Long-range Correlations in* $\sqrt{s_{NN}}$*=5.02 TeV Proton-lead Collisions with the ATLAS Detector*, Phys. Rev. Lett. **110** (2013) 182302, arXiv:1212.5198 [hep-ex].

[5] ATLAS Collaboration, *Measurement of long-range pseudorapidity correlations and azimuthal harmonics in* $\sqrt{s_{\mathrm{NN}}}$ *= 5.02 TeV proton-lead collisions with the ATLAS detector*, Phys. Rev. C **90** (2014) 044906, arXiv:1409.1792 [hep-ex].

[6] CMS Collaboration, *Evidence for Collective Multiparticle Correlations in p-Pb Collisions*, Phys. Rev. Lett. **115** (2015) 012301, arXiv:1502.05382 [nucl-ex].

[7] ATLAS Collaboration, *Measurements of long-range azimuthal anisotropies and associated Fourier coefficients for pp collisions at* $\sqrt{s}$ = 5.02 *and* 13 *TeV and p+Pb collisions at* $\sqrt{s_{\mathrm{NN}}}$ = 5.02 *TeV with the ATLAS detector*, Phys. Rev. C **96** (2017) 024908, arXiv:1609.06213 [nucl-ex].

[8] K. Dusling and R. Venugopalan, *Comparison of the color glass condensate to dihadron correlations in proton-proton and proton-nucleus collisions*, Phys. Rev. D **87** (2013) 094034, arXiv:1302.7018 [hep-ph].

[9] P. Bozek and W. Broniowski, *Collective dynamics in high-energy proton-nucleus collisions*, Phys. Rev. C **88** (2013) 014903, arXiv:1304.3044 [nucl-th].

[10] N. Borghini, P. M. Dinh, and J.-Y. Ollitrault, *A New method for measuring azimuthal distributions in nucleus-nucleus collisions*, Phys. Rev. C **63** (2001) 054906, arXiv:nucl-th/0007063 [nucl-th].

[11] A. Bilandzic, R. Snellings, and S. Voloshin, *Flow analysis with cumulants: Direct calculations*, Phys. Rev. C **83** (2011) 044913, arXiv:1010.0233 [nucl-ex].

[12] A. Bilandzic, C. H. Christensen, K. Gulbrandsen, A. Hansen, and Y. Zhou, *Generic framework for anisotropic flow analyses with multiparticle azimuthal correlations*, Phys. Rev. C **89** (2014) 064904, arXiv:1312.3572 [nucl-ex].

[13] J. Jia, M. Zhou, and A. Trzupek, *Revealing long-range multiparticle collectivity in small collision systems via subevent cumulants*, Phys. Rev. **C96** (2017) 034906, arXiv:1701.03830 [nucl-th].

[14] ATLAS Collaboration, *Observation of Long-Range Elliptic Azimuthal Anisotropies in $\sqrt{s}$ =13 and 2.76 TeV pp Collisions with the ATLAS Detector*, Phys. Rev. Lett. **116** (2016) 172301, arXiv:1509.04776 [hep-ex].

[15] CMS Collaboration, *Evidence for collectivity in pp collisions at the LHC*, Phys. Lett. B **765** (2017) 193–220, arXiv:1606.06198 [nucl-ex].

[16] P. Huo, K. Gajdošová, J. Jia, and Y. Zhou, *Importance of non-flow in mixed-harmonic multi-particle correlations in small collision systems*, Phys. Lett. **B777** (2018) 201–206, arXiv:1710.07567 [nucl-ex].

[17] ATLAS Collaboration, *Measurement of multi-particle azimuthal correlations in pp, p+Pb and low-multiplicity Pb+Pb collisions with the ATLAS detector*, Eur. Phys. J. **C77** (2017) 428, arXiv:1705.04176 [hep-ex].

[18] ATLAS Collaboration, *Measurement of multi-particle azimuthal correlations with the subevent cumulant method in pp and p+Pb collisions with the ATLAS detector at the LHC*, Phys. Rev. C **97** (2018) 024904, arXiv:1708.03559 [hep-ex].

[19] CMS Collaboration, *Observation of correlated azimuthal anisotropy Fourier harmonics in pp and pPb collisions at the LHC*, Phys. Rev. Lett. **120** (2018) 092301, arXiv:1709.09189 [nucl-ex].

[20] ATLAS Collaboration, *The ATLAS Experiment at the CERN Large Hadron Collider*, JINST **3** (2008) S08003.

[21] ATLAS Collaboration, *The ATLAS Inner Detector commissioning and calibration*, Eur. Phys. J. C **70** (2010) 787, arXiv:1004.5293 [physics.ins-det].

[22] ATLAS Collaboration, *ATLAS Insertable B-Layer Technical Design Report*, Atlas-tdr-19, 2010, https://cds.cern.ch/record/1291633, *ATLAS Insertable B-Layer Technical Design Report Addendum*, ATLAS-TDR-19-ADD-1, 2012, URL: https://cds.cern.ch/record/1451888.

[23] ATLAS Collaboration, *Performance of the ATLAS Trigger System in 2010*, Eur. Phys. J. C **72** (2012) 1849, arXiv:1110.1530 [hep-ex].

[24] ATLAS Collaboration, *Performance of the ATLAS Trigger System in 2015*, Eur. Phys. J. **C77** (2017) 317, arXiv:1611.09661 [hep-ex].

[25] ATLAS Collaboration, *Charged-particle distributions in $\sqrt{s}$=13 TeV pp interactions measured with the ATLAS detector at the LHC*, Phys. Lett. B **758** (2016) 67, arXiv:1602.01633 [hep-ex].

[26] ATLAS Collaboration, *Performance of the ATLAS Minimum Bias and Forward Detector Triggers in pPb collisions*, ATLAS-CONF-2013-104, https://cds.cern.ch/record/1624013.

[27] T. Sjöstrand, S. Mrenna, and P. Z. Skands, *A Brief Introduction to PYTHIA 8.1*, Comput. Phys. Commun. **178** (2008) 852, arXiv:0710.3820 [hep-ph].

[28] ATLAS Collaboration, *ATLAS tunes of PYTHIA 6 and Pythia 8 for MC11*, ATLAS-PHYS-PUB-2011-009, https://cds.cern.ch/record/1363300.

[29] M. Gyulassy and X.-N. Wang, *HIJING 1.0: A Monte Carlo program for parton and particle production in high-energy hadronic and nuclear collisions*, Comput. Phys. Commun. **83** (1994) 307, arXiv:nucl-th/9502021.

[30] GEANT4 Collaboration, S. Agostinelli et al., *GEANT4: A Simulation toolkit*, Nucl. Instrum. Meth. A **506** (2003) 250.

[31] ATLAS Collaboration, *The ATLAS Simulation Infrastructure*, Eur. Phys. J. C **70** (2010) 823, arXiv:1005.4568 [physics.ins-det].

[32] ATLAS Collaboration, *Measurement of forward-backward multiplicity correlations in lead-lead, proton-lead and proton-proton collisions with the ATLAS detector*, Phys. Rev. C **95** (2017) 064914, arXiv:1606.08170 [hep-ex].

[33] P. Di Francesco, M. Guilbaud, M. Luzum, and J.-Y. Ollitrault, *Systematic procedure for analyzing cumulants at any order*, Phys. Rev. C **95** (2017) 044911, arXiv:1612.05634 [nucl-th].

[34] G. Giacalone, L. Yan, J. Noronha-Hostler, and J.-Y. Ollitrault, *Symmetric cumulants and event-plane correlations in Pb + Pb collisions*, Phys. Rev. **C94** (2016) 014906, arXiv:1605.08303 [nucl-th].

[35] S. J. Das, G. Giacalone, P.-A. Monard, and J.-Y. Ollitrault, *Relating centrality to impact parameter in nucleus-nucleus collisions*, Phys. Rev. C **97** (2018) 014905, arXiv:1708.00081 [nucl-th].

[36] ATLAS Collaboration, *Measurement of the azimuthal anisotropy for charged particle production in* $\sqrt{s_{NN}}$ = 2.76 *TeV lead-lead collisions with the ATLAS detector*, Phys. Rev. C **86** (2012) 014907, arXiv:1203.3087 [hep-ex].

[37] P. Bozek, W. Broniowski, and J. Moreira, *Torqued fireballs in relativistic heavy-ion collisions*, Phys. Rev. C **83** (2011) 034911, arXiv:1011.3354 [nucl-th].

[38] L.-G. Pang, G.-Y. Qin, V. Roy, X.-N. Wang, and G.-L. Ma, *Longitudinal decorrelation of anisotropic flows in heavy-ion collisions at the CERN Large Hadron Collider*, Phys. Rev. C **91** (2015) 044904, arXiv:1410.8690 [nucl-th].

[39] CMS Collaboration, *Evidence for transverse momentum and pseudorapidity dependent event plane fluctuations in PbPb and pPb collisions*, Phys. Rev. C **92** (2015) 034911, arXiv:1503.01692 [nucl-ex].

[40] ATLAS Collaboration, *Measurement of longitudinal flow de-correlations in Pb+Pb collisions at* $\sqrt{s_{\mathrm{NN}}}$ = 2.76 *and 5.02 TeV with the ATLAS detector*, Eur. Phys. J. C **78** (2018) 142, arXiv:1709.02301 [nucl-ex].

[41] ATLAS Collaboration, *Measurement of event-plane correlations in* $\sqrt{s_{NN}}$ = 2.76 *TeV lead-lead collisions with the ATLAS detector*, Phys. Rev. C **90** (2014) 024905, arXiv:1403.0489 [hep-ex].

[42] ATLAS Collaboration, *Measurement of the correlation between flow harmonics of different order in lead-lead collisions at* $\sqrt{s_{NN}}$*=2.76 TeV with the ATLAS detector*, Phys. Rev. C **92** (2015) 034903, arXiv:1504.01289 [hep-ex].

[43] ALICE Collaboration, J. Adam et al., *Correlated event-by-event fluctuations of flow harmonics in Pb-Pb collisions at* $\sqrt{s_{NN}}$ = 2.76 *TeV*, Phys. Rev. Lett. **117** (2016) 182301, arXiv:1604.07663 [nucl-ex].

Appendix

A Improvement to the template fit procedure

In order to separate the long-range ridge from other non-flow sources, especially dijets, the ATLAS Collaboration developed a template fitting procedure described in Refs. [7,14]. The analysis first constructs a $\Delta\phi$ distribution of particle pairs with large pseudorapidity separation $|\Delta\eta| > 2$, so called "per-trigger" particle yield, $Y(\Delta\phi)$, for a given $N_{\rm ch}^{\rm rec}$ range. The $|\Delta\eta| > 2$ requirement suppresses the intra-jet and other short-range correlations, and resulting $Y(\Delta\phi)$ distributions are known to be dominated by away-side jet correlations in small collision systems [4,5,14]. This away-side non-flow component is peaked at $\Delta\phi \sim \pi$, and leads to a significant bias to the flow coefficients v_n, especially for the odd harmonics.

To subtract the away-side jet correlations, the measured $Y(\Delta\phi)$ distribution in a given $N_{\rm ch}^{\rm rec}$ interval is assumed to be a sum of a scaled "peripheral" distribution $Y(\Delta\phi)^{\rm peri}$, obtained for low multiplicity events $N_{\rm ch}^{\rm rec} < 20$, and a constant pedestal modulated by $\cos(n\Delta\phi)$ for $n \geq 2$ [7,14]:

$$Y(\Delta\phi) = F\, Y(\Delta\phi)^{\rm peri} + G^{\rm tmp}\left(1 + 2\sum_{n=2}^{\infty} v_n\{2,{\rm tmp}\}^2 \cos n\Delta\phi\right). \tag{17}$$

The scale factor F and pedestal $G^{\rm tmp}$ are fixed by the fit, and $v_n\{2,{\rm tmp}\}$ are calculated from a Fourier transform. On the other hand, both $Y(\Delta\phi)$ and $Y(\Delta\phi)^{\rm peri}$ contain a dijet component and flow component:

$$Y(\Delta\phi) = Y(\Delta\phi)_{\rm jet}^{\rm cent} + G^{\rm cent}\left(1 + 2\sum_{n=2}^{\infty} v_n\{2\}^2 \cos n\Delta\phi\right). \tag{18}$$

$$Y(\Delta\phi)^{\rm peri} = Y(\Delta\phi)_{\rm jet}^{\rm peri} + G^{\rm peri}\left(1 + 2\sum_{n=2}^{\infty} v_n\{2,{\rm peri}\}^2 \cos n\Delta\phi\right). \tag{19}$$

With the assumption that the shape of the dijet component is independent of $N_{\rm ch}^{\rm rec}$, and the magnitudes of the dijet component are related by the scale factor F: $Y(\Delta\phi)_{\rm jet}^{\rm cent} = FY(\Delta\phi)_{\rm jet}^{\rm peri}$, Eq.(17) can be written as:

$$Y(\Delta\phi) = Y(\Delta\phi)_{\rm jet}^{\rm cent} + (G^{\rm tmp} + FG^{\rm peri}) + 2\sum_{n=2}^{\infty}\left(G^{\rm tmp} v_n\{2,{\rm tmp}\}^2 + FG^{\rm peri} v_n\{2,{\rm peri}\}^2\right)\cos n\Delta\phi. \tag{20}$$

Comparing with Eq. (18), one obtains $G^{\rm cent} = G^{\rm tmp} + FG^{\rm peri}$ and the following relation:

$$v_n\{2\}^2 = v_n\{2,{\rm tmp}\}^2 - \frac{F\,G^{\rm peri}}{G^{\rm cent}}\left(v_n\{2,{\rm tmp}\}^2 - v_n\{2,{\rm peri}\}^2\right), \tag{21}$$

which shows that $v_n\{2,{\rm tmp}\}$ from the template fit differs from the true $v_n\{2\}$ by a correction term that vanishes if and only if $v_n\{2\}$ is independent of $N_{\rm ch}^{\rm rec}$. Since the true flow harmonics in the peripheral interval $v_n\{2,{\rm peri}\}$ are unknown in principle, the correction is applied starting from the third lowest $N_{\rm ch}^{\rm rec}$ interval ($40 \leq N_{\rm ch}^{\rm rec} < 60$) in this analysis, by using $v_n\{2,{\rm tmp}\}$ of the second $N_{\rm ch}^{\rm rec}$ interval ($20 \leq N_{\rm ch}^{\rm rec} < 40$) as an estimate of the true flow harmonics. Since the non-flow primarily affects the odd harmonics, the $v_3\{2,{\rm tmp}\}^2$ may become negative in the first few $N_{\rm ch}^{\rm rec}$ intervals in pp collisions. In such cases, the correction starts from the second $N_{\rm ch}^{\rm rec}$ interval with positive $v_3\{2,{\rm tmp}\}^2$ ($60 \leq N_{\rm ch}^{\rm rec} < 80$) by using $v_3\{2,{\rm tmp}\}$ from the previous $N_{\rm ch}^{\rm rec}$ interval ($40 \leq N_{\rm ch}^{\rm rec} < 60$).

One important feature of the template fit analysis is the assumption that the dijet component $Y(\Delta\phi)_{\rm jet}$ is independent of $\langle N_{\rm ch}\rangle$. In Ref. [7], the uncertainty associated with this assumption is studied by changing the default peripheral interval from $N_{\rm ch}^{\rm rec} < 20$ to $N_{\rm ch}^{\rm rec} < 10$ and $10 \le N_{\rm ch}^{\rm rec} < 20$. It was found that the $v_n\{2, {\rm tmp}\}$ values are relatively insensitive to the choice of the peripheral interval for $n = 2$ and $n = 4$, but the sensitivity is much larger for $n = 3$. This finding is reproduced in Figure 6 for pp collisions, which shows that the $v_3\{2, {\rm tmp}\}^2$ obtained via Eq. (17) differs substantially for the different $N_{\rm ch}^{\rm rec}$ ranges.

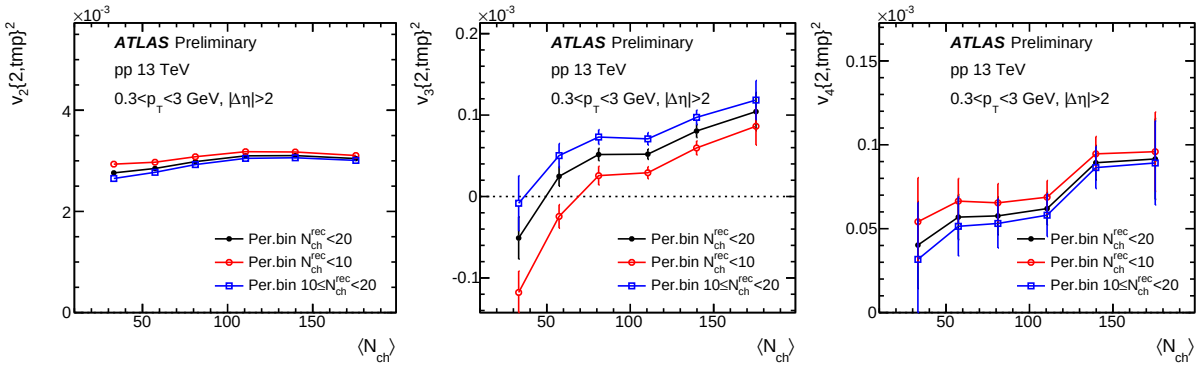

Figure 6: The values of $v_n\{2, {\rm tmp}\}^2$ obtained following the template fit procedure given in Eq. (17) [7] in pp collisions for $n = 2$ (left panel), $n = 3$ (middle panel) and $n = 4$ (right panel). In each panel, the values are calculated for three peripheral $N_{\rm ch}^{\rm rec}$ intervals: $N_{\rm ch}^{\rm rec} < 20$, $N_{\rm ch}^{\rm rec} < 10$ and $10 \le N_{\rm ch}^{\rm rec} < 20$. Only statistical uncertainties are shown.

In addition to the template fit with and without the above mentioned correction procedure, ATLAS and CMS Collaborations also calculated directly the $v_n\{2\}$ values via a Fourier transform of the $Y(\Delta\phi)$ distribution without dijet subtraction [7, 19]. The differences between the direct Fourier transform and template fit reflect mainly the away-side jet contribution subtracted by the template fit procedure, and therefore give a sense of the magnitude of unknown systematics associated with the template fit procedure. If these differences are too large, the $v_n\{2, {\rm tmp}\}$ values may be sensitive to the systematic effects associated with the assumption that the shape of $Y(\Delta\phi)_{\rm jet}$ is independent of $N_{\rm ch}^{\rm rec}$.

Figure 7 compares the $v_n\{2\}$ in $0.3 < p_{\rm T} < 3$ GeV obtained from $Y(\Delta\phi)$ using three methods: a direct Fourier transform (solid circles), a template fit (open circles) and a template fit corrected for the bias (open squares), as described above. The systematic uncertainties for the template fit results are nearly the same as those from Ref. [7]. Figure 7 shows that the changes introduced by the correction procedure described above are small in all cases and for all harmonics. The values of the even order harmonics, v_2 and v_4, are also quite similar to those obtained from the direct Fourier transformation, reflecting the fact that the dijet correlations have very small influence on the even-order harmonics. On the other hand, significant differences are observed between the direct Fourier transform and template fit for v_3 especially in the pp collisions due to influence of $Y(\Delta\phi)_{\rm jet}$, a trend observed and discussed already in Refs. [7, 15]. The template fit procedure is able to subtract the dijet correlations and change the sign of v_3, but also introduces large uncertainty associated with the procedure. As discussed in Section 8.2, the behaviors of the symmetric cumulants ${\rm sc}_{2,3}\{4\}$ in Figure 4 and normalized cumulants ${\rm nsc}_{2,3}\{4\}$ in Figure 5 in pp collisions, suggest that the v_3 values from the template fit procedure are significantly underestimated due to the presence of large residual non-flow bias. In contrast, the differences of v_3 between the direct Fourier transform and template fit are much smaller in the p+Pb and the Pb+Pb collisions, except in the very low $\langle N_{\rm ch}\rangle$ region. Therefore, the v_3 values in p+Pb and Pb+Pb systems extracted from the template fit

procedure are expected to be less affected by the dijets.

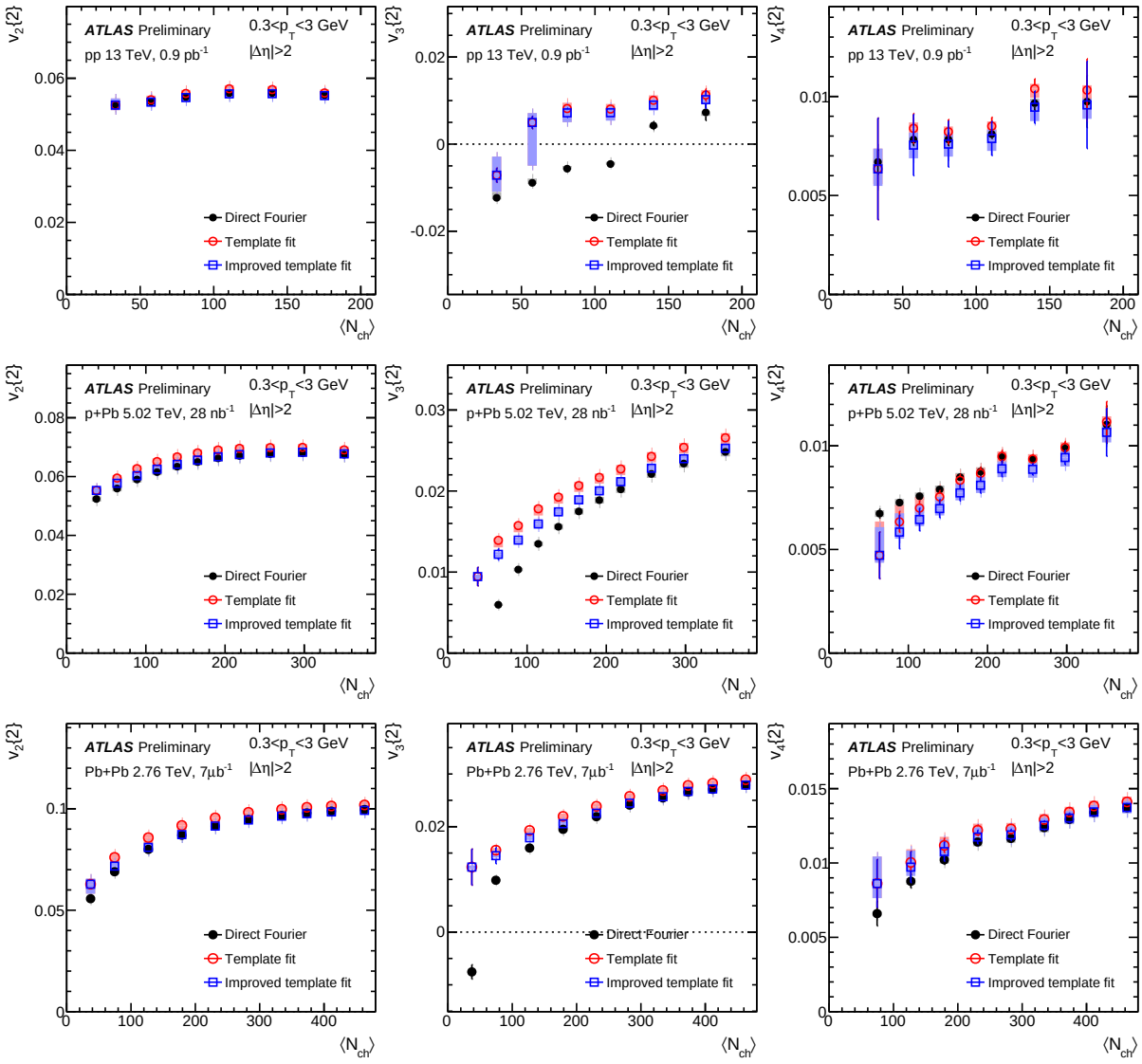

Figure 7: The v_2 (left column), v_3 (middle column) and v_4 (right column) obtained from two-particle correlations in $0.3 < p_{\mathrm{T}} < 3$ GeV in pp (top row), p+Pb (middle row) and Pb+Pb (bottom row) collisions. In each panel, they are compared between three methods: direct Fourier transformation (solid circles), template fit (open circles) and the improved template fit (open squares). The error bars and shaded boxes represent the statistical and systematic uncertainties, respectively.

B Additional figures

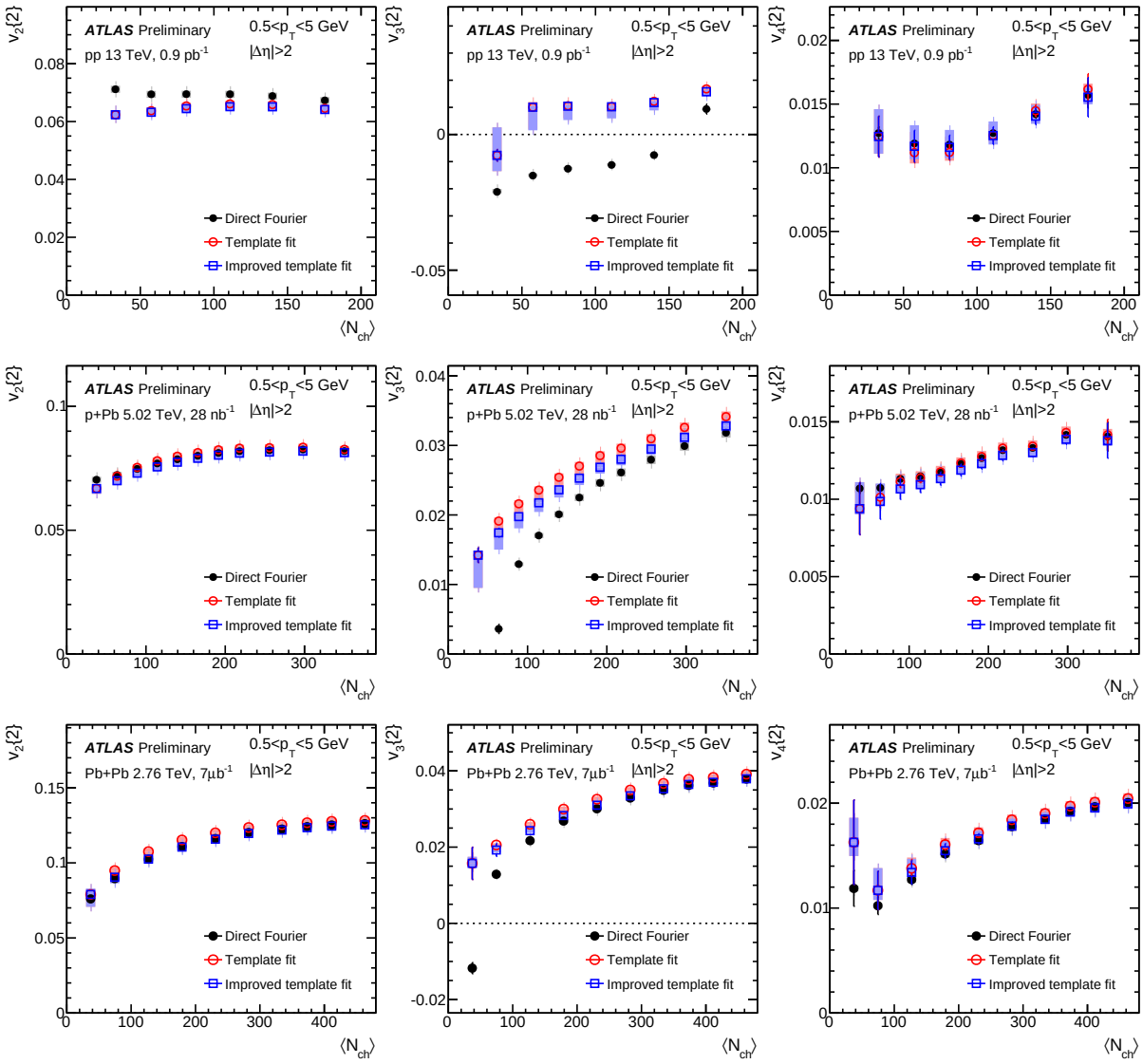

Figure 8: The v_2 (left column), v_3 (middle column) and v_4 (right column) obtained from two-particle correlations in $0.5 < p_{\mathrm{T}} < 5$ GeV in pp (top row), p+Pb (middle row) and Pb+Pb (bottom row) collisions. In each panel, they are compared between three methods: direct Fourier transformation (solid circles), template fit (open circles) and improved template fit (open squares). The error bars and shaded boxes represent the statistical and systematic uncertainties, respectively.

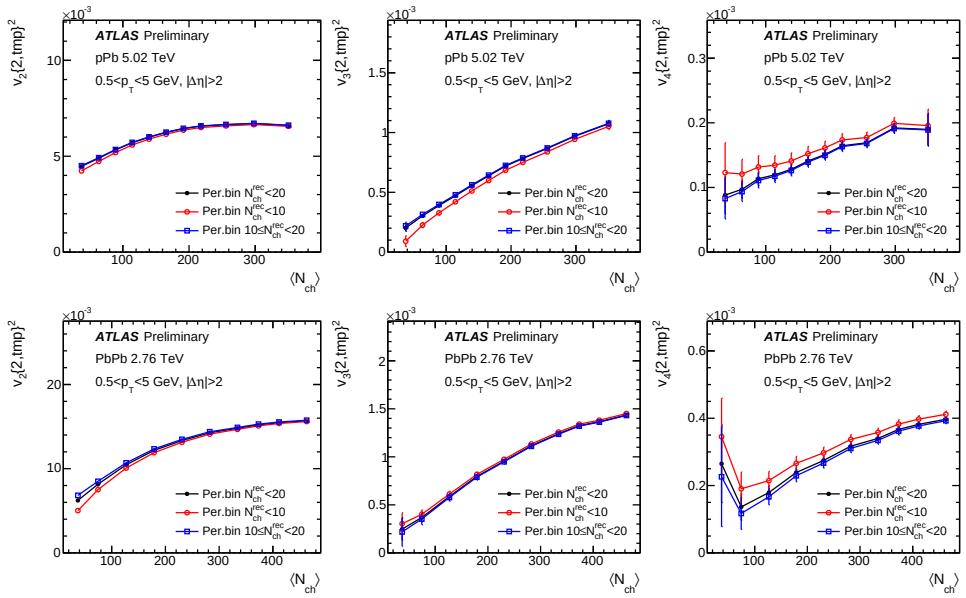

Figure 9: The values of $v_n\{2,\mathrm{tmp}\}^2$ obtained following the template fit procedure [7] in p+Pb (top row) and low-multiplicity Pb+Pb (bottom row) collisions for $n = 2$ (left panels), $n = 3$ (middle panels) and $n = 4$ (right panels). In each panel, the values are calculated for three peripheral $N_{\mathrm{ch}}^{\mathrm{rec}}$ intervals: $N_{\mathrm{ch}}^{\mathrm{rec}} < 20$, $N_{\mathrm{ch}}^{\mathrm{rec}} < 10$ and $10 \leq N_{\mathrm{ch}}^{\mathrm{rec}} < 20$. The lines connecting the points serve to distinguish different datasets. Only statistical uncertainties are shown.

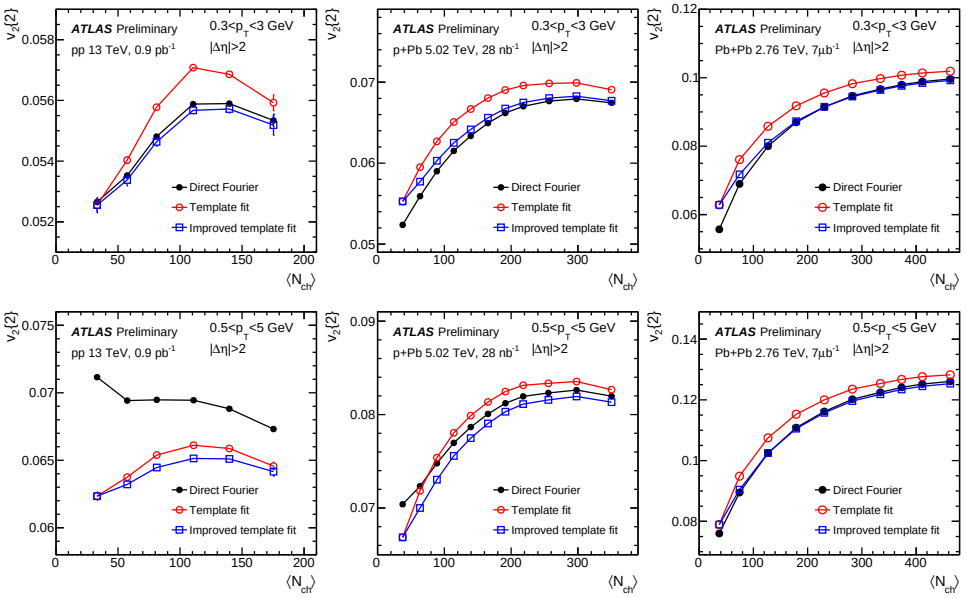

Figure 10: The values of $v_n\{2\}$, zoomed in a narrow y-axis range, obtained from two-particle correlations in $0.3 < p_{\mathrm{T}} < 3$ GeV (top row) and $0.5 < p_{\mathrm{T}} < 5$ GeV (bottom row) in pp (left panels), p+Pb (middle panels) and low-multiplicity Pb+Pb (right panels) collisions. In each panel, they are compared between three methods: direct Fourier transformation (solid circles), template fit (open circles) and the improved template fit (open squares). Only statistical uncertainties are shown.

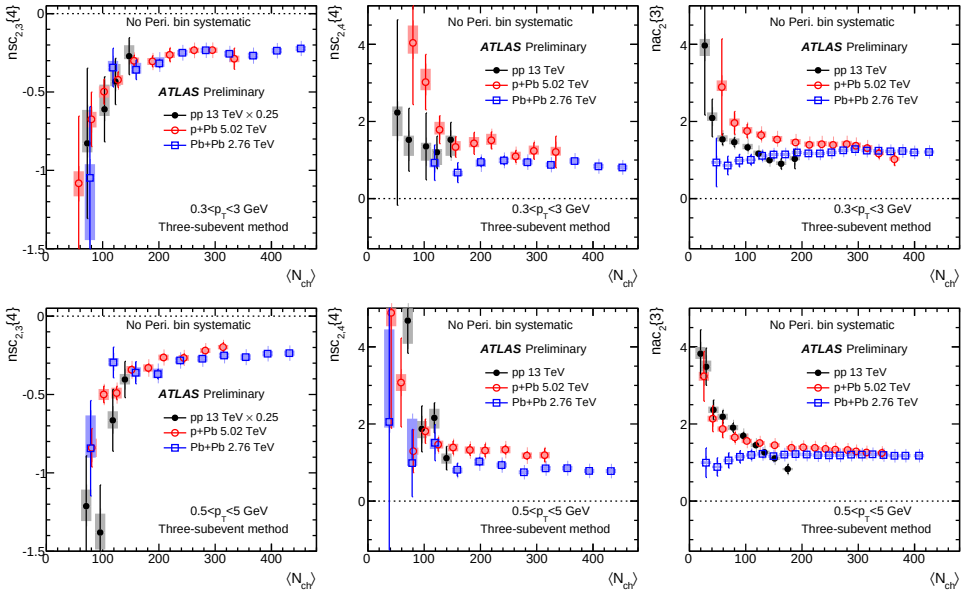

Figure 11: The $\langle N_{\rm ch}\rangle$ dependence of $\mathrm{nsc}_{2,3}\{4\}$ (left panels), $\mathrm{nsc}_{2,4}\{4\}$ (middle panels) and $\mathrm{nac}_2\{3\}$ (right panels) in $0.3 < p_{\rm T} < 3$ GeV (top row) and $0.5 < p_{\rm T} < 5$ GeV (bottom row) obtained for pp collisions (solid circles), p+Pb collisions (open circles) and low-multiplicity Pb+Pb collisions (open squares). The error bars and shaded boxes represent the statistical and systematic uncertainties, respectively. Comparing to Figure 5, the $\mathrm{nsc}_{2,3}\{4\}$ data in pp collisions in the left panels have been scaled down by a factor of 4, and uncertainties of $\langle v_n^2\rangle$ associated with the choice of peripheral $N_{\rm ch}^{\rm rec}$ intervals are not included.

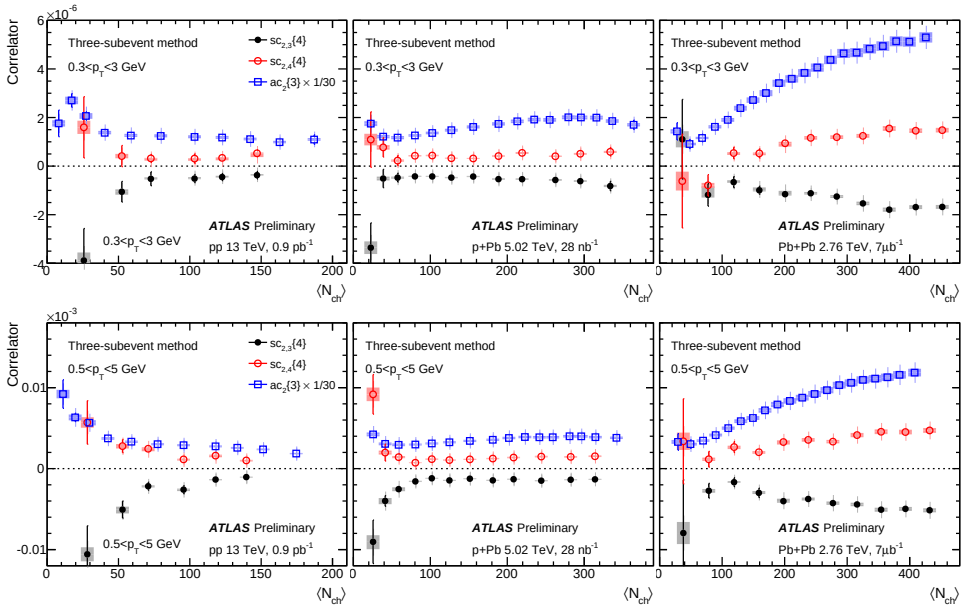

Figure 12: The $\langle N_{\rm ch}\rangle$ dependence of $\mathrm{sc}_{2,3}\{4\}$ (solid circles), $\mathrm{sc}_{2,4}\{4\}$ (open circles) and $\mathrm{ac}_2\{3\}$ (open squares) in $0.3 < p_{\rm T} < 3$ GeV (top row) and $0.5 < p_{\rm T} < 5$ GeV (bottom row) obtained for pp collisions (left panels), p+Pb collisions (middle panels) and low-multiplicity Pb+Pb collisions (right panels). The error bars and shaded boxes represent the statistical and systematic uncertainties, respectively. The $\mathrm{ac}_2\{3\}$ data have been scaled down by a factor of 30.